Masses and Radii of MML 48:
A New Pre-Main Sequence Eclipsing Binary

Thesis submitted in partial fulfillment of the requirement for

Honors in

Physics

Max Brodheim

Adviser, Leslie Hebb **November 5, 2019**

Contents

1 Introduction

The work presented in this thesis is primarily concerned with the observation and analysis of a pre-main sequence eclipsing binary star system in the southern sky named MML 48. While discussing the components of this project, it is necessary to have an understanding of the concepts, motivations, and terminology behind each element of the research conducted. This introduction serves to provide a basic background on the formation of stars, the study of how they evolve over time, a physical analysis of eclipsing binaries, an overview of the the computational modeling program PHOEBE 2.1 and its role in this research, and an overview of the subject of this paper, the star system MML 48.

1.1 Stellar Birth

Most stars function following a familiar process: a big ball of gas has a core that is so hot and dense that fusion between light elements occurs, generating extraordinary amounts of energy. The energy produced from the fusion in the core balances out the gravitational forces pulling the gas inward, resulting in a star. Stars that fuse elements together to remain stable are considered fully formed, 'adult' stars [2]. At some point in its life, a star will either evolve into a red giant or supergiant before collapsing into itself, or slowly fade into a white dwarf, where its life as a star ends [2, 4].

The process that leads from a star being born to it becoming fully formed requires more investigation. While the specifics of stellar evolution remain uncertain, there is a generally agreed upon pattern of development that is presented here [4]. All stars begin as an enormous cloud of interstellar gas and dust with a makeup of approximately 70% hydrogen, 28% helium, and 2% heavier elements [2]. These clouds typically maintain an equilibrium, referred to as *hydrostatic equilibrium*, between the weak gravitational attraction between each particle that pulls the cloud together and the thermal energy of each particle that pushes back out. This thermal energy resisting the collapse of the cloud is referred to as the *thermal pressure*. Through the study of small deviations to the hydrostatic equilibrium present in these clouds, early researchers were able to make some insights into some of the conditions required for these interstellar clouds to collapse into stars [13]. This research resulted in the description of *Jean's Criterion*, which provides a strict mathematical limit on which clouds will or will not collapse. If a cloud happens to be particularly cold and dense, then simple molecules are able to form. These molecules cause the density of the clouds to get much greater than would be possible for hotter interstellar clouds, which in turn gives the clouds the mass needed to overcome the Jean's Criterion and collapse under its own gravity, and form a star [2, 4]. This collapse is by no means a smooth process: because each molecule of gas in the cloud has its own angular momentum with respect to the center of the cloud, the formed star will be spinning extremely quickly. Additionally, collisions between those molecules before they hit the star cause the cloud's contents to form into an *accretion disk*, which is a hot, dense disk of dust and gas that forms around the star as the material falls in [4].

Once the cloud starts to contract, the gravitational potential energy of the particles is converted into thermal pressure that opposes the contraction. Here again, the properties of molecular clouds (as opposed to primarily elemental clouds) help in star formation. The molecules present in the clouds, such as carbon monoxide, can absorb the energy and release it in the form of photons of a much lower energy than those emitted by H_2 [4]. This radiation of energy is a requirement for stellar formation: without it, the thermal pressure would build up until the cloud's gravitational potential found a new equilibrium point. Incidentally, this radiation emission is also what enables astronomers to study these clouds directly, as this light from the molecules (usually carbon monoxide) can be observed from the Earth [2].

Eventually, an interstellar cloud will get dense and hot enough that those photons cannot easily penetrate out of the cloud, which leads to a rapid increase in the temperature and pressure in the cloud [2]. The surface temperature of the core of the clouds reach levels

Figure 1: False color image of the Carina Nebula (also called the Key-Hole Nebula) taken by the Hubble Space Telescope in 1999. The dark knots and wisps throughout the image are dense clouds of interstellar dust and gas. Although the clouds in this image are much denser than the clouds that form protostars, it is expected that nearby stars in the same nebula will disperse this gas before any of it can form into a protostar. Image Source: NASA, Hubble Heritage, AURA/STScI.

comparable to those of a fully formed star, which produces similar luminosities. Molecular clouds that reach this phase have now become *protostars* [2].

These stars, while extremely hot, are not yet dense or hot enough to reliably fuse hydrogen into heavier elements through the proton-proton chain, so they need another source of energy [4]. This energy comes in the form of material falling onto the core from the rest of the cloud. As the free falling material from the cloud collides with the hydrostatically stable core, it rapidly decelerates and releases large amounts of thermal energy [4]. This provides the energy needed to maintain stability, as the temperature of the core slowly rises. Through various processes, the core undergoes several further contractions, but relies primarily on material collapsing into the core from the accretion disk for energy [4]. It is at this point in protostellar development that there are a lot of unanswered questions about how stellar development progresses. More attention will be given to the properties that govern the transition from protostar to pre-main sequence in Section 1.3.1.

During this phase of contraction, all pre-main sequence stars undergo a set of changes that were first theorized by Chushiro Hayashi in 1961. In his model, which implemented one of the first analysis of both hydrostatics and convective currents in protostars, Hayashi demonstrated that there is a phase in protostellar evolution in which the effective temperature of a star increases slightly, while the luminosity decreases significantly [4]. In Figure 2, several protostars of varying masses are shown as they evolve over time.

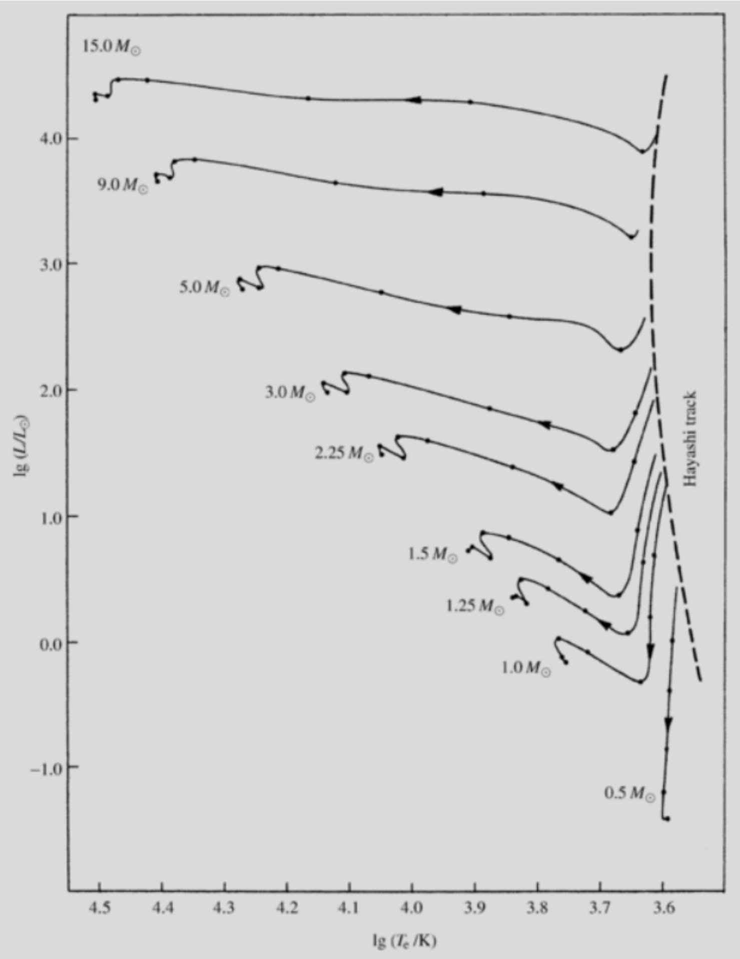

Figure 2: Various pre-main sequence stellar evolution paths. Each track begins at the Hayashi Track (the long dashed line), and moves left until the star is deposited on the main sequence. The mass of each star is given at the end of each track. On the right side of the Hayashi Track, stellar formation cannot occur [4]. Image Source: *Fundamental Astronomy* [15].

If we plot the observable quantities of luminosity (the brightness of the star) and temperature, this takes the form of a vertical line [4]. This kind of plot is referred to as a Hertzsprung-Russell diagram, and is explained in full in Section 1.2.1. This model was later determined to be insufficient for fully predicting the behavior of real-life observed targets later in their evolution, but it provided some useful information about young pre-main sequence stars [7]. Specifically, Hayashi demonstrated that there were ‘allowed’ and ‘disallowed’ regions on the H-R diagram in which stability can or can not occur. If the effective temperature of a star is low enough for a given luminosity, there is no way that a protostar could emit the amount of light that it does. In Figure 2, the limit between the allowed and disallowed region is displayed as the *Hayashi Track* [4].

Eventually, the temperature gets high enough for deuterium to begin fusing, which provides additional energy to the star, enough to slow but not stop the collapse of the cloud [4]. Once all of the deuterium (which fuses at much lower temperatures than the H_2 that fuels the proton-proton chain present in fully-formed stars) is exhausted, the star reaches a somewhat stable state [4]. The temperature inside the protostar slowly rises until early steps in the proton-proton fusion chain are made, and heavier elements begin to form. Once a star is fusing hydrogen into helium in its core, the star’s luminosity and temperature will line up with the main sequence, and the star’s birth is considered complete [4].

1.2 Stellar Evolution

With an understanding of how stars form, we can move on to trying to describe how observable quantities of stars change over time. Just as there is a general pattern that stars follow during their formation, there is a well-accepted set of changes that most stars undergo throughout their lives [4]. In the mid-to-late 1800’s and early 1900’s advancements in photography and spectroscopy enabled astronomers to collect vast sums of new data about stars, which spurred progress into our understanding how they function [3].

1.2.1 The Hertzsprung-Russell Diagram

Between 1910 and 1915, a crucial jump forward in understanding the general behavior of stars in the sky was made in the form of the so-called *Hertzsprung-Russell (H-R) Diagram*, pictured in Figure 3 [11, 25]. This diagram, enabled by the extensive research and cataloguing of Annie Jump Cannon and then Antonia Maury, demonstrates the relationship between the color (and by extension the surface temperature) of a star, and its luminosity [18, 2]. In turn, the luminosity of a star is determined by the Stefan-Boltzmann Equation, which states that the luminosity of a spherical star can be expressed as:

$$L = 4\pi R^2 \sigma T^4, \tag{1}$$

where L is the luminosity, R is the radius of the star, σ is the Stefan-Boltzmann constant, and T is the effective temperature (essentially the surface temperature) of the star. In other words, the luminosity of a star is directly tied to its radius and surface temperature, which means an H-R diagram also provides a relationship between the radius and temperature of a star [2].

This diagram provided a much needed framework for both modeling and observational efforts: as new data was acquired about the age and mass of stars, more trends became apparent in the diagram, which in turn gave theorists more structure to seek out [4]. For example, astronomers initially theorized that because hotter stars had been observed to be brighter (a relationship that holds for the main sequence), they might all start as extremely hot blue stars, and then gradually burn off their mass, cooling off into red stars [4]. The H-R diagram provided the organization needed to see that the presence of White Dwarfs and Giants demonstrated that there wasn't a universal transition from hot to cool stars with relation to radius. These inquiries formed the first real studies of stellar evolution, and by extension the first modern investigations into stellar evolution [4].

Another leap forward was made when astronomers discovered that the primary deter-

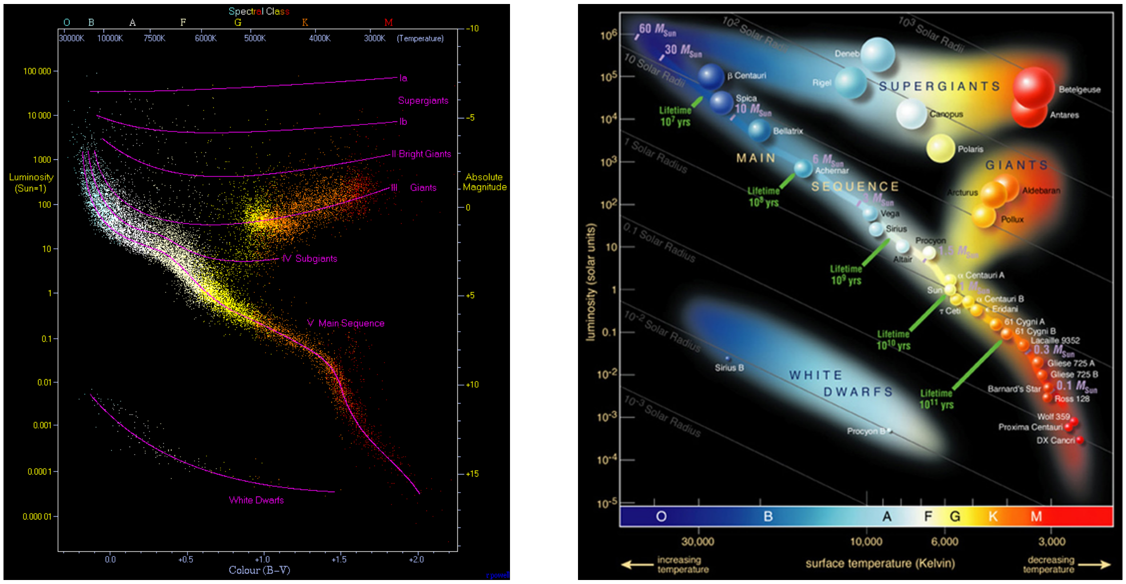

Figure 3: Two Hertzsprung-Russel Diagrams. Each point on the left diagram denotes the location of a real observed star on the H-R diagram. The purple lines outline the different paths that observed stars tend to lie on, most notable of which is the heavily-populated main sequence. The graphic on the right displays a stylized version of this data, with a few added elements. Since the luminosity of a star is determined by its temperature and radius, an H-R diagram can also be used to examine stellar radii, shown as grey diagonal lines. On both of the diagrams, the x-axis represents the surface temperature of a star (moving from hot to cool) and the y-axis represents the luminosity. Left Image Source: Richard Powell [22]. Right Image Source: NASA/JPL [2].

mination of a star's temperature was directly tied to that star's mass [2]. This relationship is presented in the purple text of the right graphic in Fig. 3. With this, astronomers had a framework for understanding how the radius and mass of stars were connected. Arguably the most significant discovery associated with the H-R diagram was that of the main-sequence, or the line of stars stretching from the upper-left to lower-right of the H-R diagram. Anywhere from 80-90 % of all stars lie on this line, and modeling how stars find their way onto that line, and eventually slip off it, forms the primary focus of stellar evolution modeling up to the current day [4].

It is important to recognize explicitly that the H-R diagram does not provide any direct information about how a star changes over time, it merely is a way to organize the stars that we observe. In order to do that, one needs to develop a model stellar evolution.

1.2.2 Contemporary Stellar Evolution Models

By the early 1960's, significant improvements were made to the simplest models that had emerged to explain the trends seen in the H-R diagram [4]. Physical phenomena ranging in scale from the very method of fusion at the heart of stars, to the convection currents that carried energy away from the cores, to the ionization state of hydrogen in the atmosphere of stars were integrated into models, yielding more complicated and reliable predictions for stellar behavior. Over the ensuing decades, more phenomena were identified as being important to the evolution of stars, including magnetic fields, angular momentum, and mass ejections, among many others [4].

Contemporary models typically take the form of large lookup tables. An astronomer can input a set of initial parameters (such as effective temperature, mass, radius, and age), and then look up the corresponding values for a later stage in that stars life. These evolution tables differ from H-R diagrams in many ways, but most crucially, they give researchers a model for a single star over time, while an H-R diagram displays information about many stars at one single time. Of course, stellar evolution models must agree with the H-R diagram where applicable, but one must not conflate one as the other.

1.2.3 Importance of Stellar Evolution Models to Astronomy

Stellar evolution models are present in almost every field in the astronomy community. As an example, an exoplanet researcher would need to know the mass of a target star in order to determine the mass of an exoplanet around it, which cannot typically be directly measured. Instead, the mass can be determined by comparing the star's luminosity and temperature to stellar evolution models. Another example can be found in someone researching galactic structure, who might need to have accurate measurements of the density of mass in a given region. This can be estimated with stellar evolution models [26, 7].

There are several properties of stars beyond the mass and radius that are determined through the use of stellar evolution models. For example, age determinations of most young stars rest almost entirely on the use of modeling [7]. These age determinations are essential to research about how the clouds that form stars dissipate over time, how long it takes gas giant planets like Jupiter to form around stars, and other age-determined properties of stars [26]. Additionally, prediction of magnetic activity (primarily in the form of star spots) is important to account for while observing pre-main sequence targets. The ubiquity of the use of stellar evolution models is the reason that they attract so much attention in the astronomical research community. Adding functionality to these models, in terms of integrating additional physical phenomena or increasing their precision, has significant ramifications for the astronomy community as a whole.

1.2.4 Shortcomings of Stellar Evolution Models

While stellar evolution models have and continue to develop over the course of the last century, they still require improvement. This becomes apparent with both advances in the theory behind stellar structure and the discovery of inconsistencies between observations and predictions from models.

There are many different physical processes that have yet to be integrated into stellar evolution models than can be counted. However, there are a few specific areas that are attracting special attention in contemporary research. As stated in D'Antona's 2017 paper *From protostellar to pre-main-sequence evolution*, these include “deuterium burning, disk accretion/mass loss..., [and] realistic surface boundary conditions” [7]. Additionally, “convection..., magnetohydrodynamics..., refining nuclear reaction rates..., dynamic atmospheric opacities..., and the effects of rotation” are important factors that need further investigation [8, 4]. While modern models do implement some of these phenomena into their calculations, we can tell that they are insufficient to fully predict pre-main sequence stellar behavior by comparing the outputs of these models to observations. For example, models do not yet fully explain the strong convection-inhibiting magnetic fields that might be present in pre-main sequence stars. D'Antona points out that if these magnetic fields are important to pre-main sequence stars, then there are likely no accurate models for these types of stars [7].

In 2014, Stassun et. al conducted such a comparison using several well-accepted stellar evolution models. This review concluded that the existing models were severely lacking: for stars (both main sequence and pre-main sequence) below 1 $M_\odot$, the error rate for the models ranged from 50-100% [26]. Furthermore, the errors associated with the modeling of low mass stars were compounded when low mass pre-main sequence stars were considered [26]. A more detailed treatment of pre-main sequence stellar evolution models is given in the following section.

1.3 Pre-Main Sequence Stars

Up to this point, I have discussed the life cycle of pre-main sequence stars and models that allow for the prediction of stellar behaviors over time. The intersection of these two topics, the study of how pre-main sequence stars evolve over time, is the focus of a lot of research, as an understanding of how young stars become fully formed is essential to forming a full picture of stellar evolution.

1.3.1 Stellar Evolution Models and Pre-Main Sequence Stars

One common approach to modeling young stars is to take stellar evolution models for less exotic main sequence stars, and examine what outputs they produce for very young ages. This approach would appear to make sense: the widely accepted models mostly agree for main-sequence stars, so they should agree going backwards. However, as mentioned earlier in Section 1.2.4, a review of stellar evolution models in 2014 found that when it comes to modeling low mass pre-main sequence stars, existing models leave a lot to improve on. In Figure 4, the effectiveness of 6 different models is displayed. While some of the models (Pisa, Dartmouth 2008, and Dartmouth 2014) do a decent job of modeling observed behaviors, demonstrated by the closeness of each point to 0 on the y-axis, all of the models have significant room for improvement [26]. Of all of the models used, Pisa would be expected to perform the best, as it was specifically designed for use with pre-main sequence stars [26].

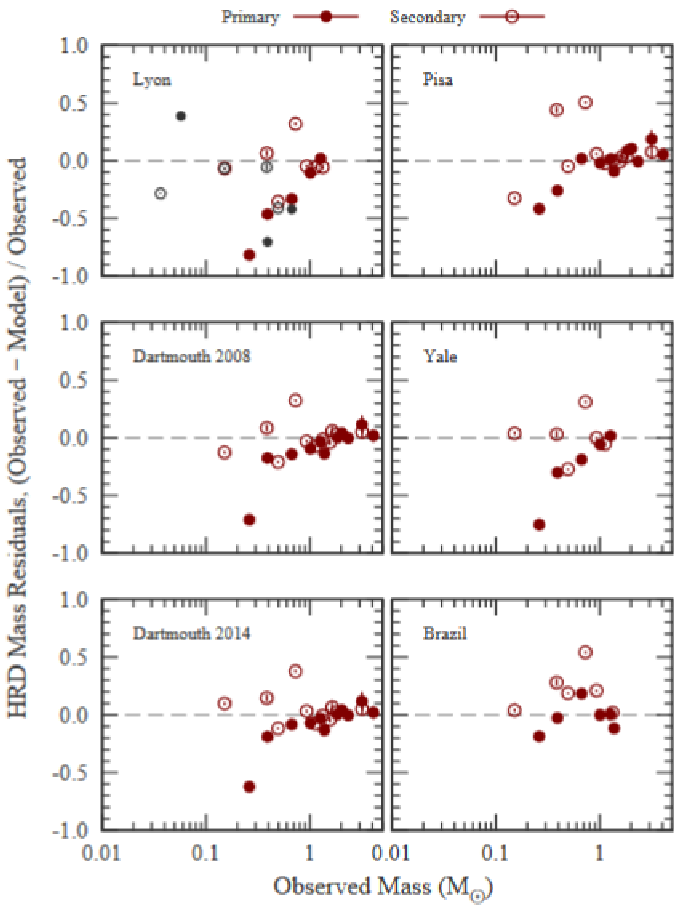

Figure 4: Various low-mass pre-main sequence eclipsing binaries with mass measurements were modeled using 6 different stellar evolution models. This plot shows the mass of each star on the x-axis, and a measurement of the agreement between 6 different models with that mass on the y-axis. A negative value on the y-axis indicates an over-estimation of mass. Image Source: *Empirical Tests of Pre-Main-Sequence Stellar Evolution Models with Eclipsing Binaries*, Stassun et. al.

One element of the review that is of particular relevance to this research project is the small number of available pre-main sequence stars with known masses and radii: there were only 13 suitable candidates for this study in 2014. While there have been more mass and radius measurements for pre-main sequence stars since the publication of that document, there is a pressing need for additional stars to be analyzed [7].

1.3.2 Difficulties in Observing Pre-Main Sequence Stars

Many of the very processes that make pre-main sequence stars so difficult to model also make them difficult to observe scientifically. Firstly, astronomers know that accretion disks play a large role in the formation of pre-main sequence stars [4, 25]. These accretion disks can be difficult to tell apart from magnetic activity on the star's surface, which can make painting a clear picture of what is going on inside the star very difficult [26]. Additionally, the clouds that form stars take a long time to fully collapse or dissipate, which means that any observation from the Earth has the potential to be obstructed by an unknown quantity of matter. This can throw off spectroscopic research into the makeup of the outer atmosphere of pre-main sequence stars, as well as impact photometric luminosity measurements [7, 26]. Finally, stars do not typically form in isolation as I described earlier. Rather, they form in groups from large fragmenting gas clouds in what are referred to as *star forming regions* [4]. The remnants of these clouds can introduce a large amount of uncertainty as to how much light emitted from those stars is mutated by the gas it has to pass through on its way to the Earth [26]. All of these factors contribute to a general lack of certainty about the behavior of pre-main sequence stars as a whole.

1.4 Eclipsing Binaries

In order to develop a detailed understanding of the physical structure and evolution of stars, we need to know some of their physical characteristics. Using observables like spectra, pass-band luminosities, and parallax, we can determine extremely useful characteristics of a star, such as its effective temperature, luminosity, radius, elemental composition, and distance from Earth [4]. However, in order to get a direct measurement of mass, we need to observe the star interacting with some other gravitationally bound object [14].

When two or more stars orbit a common center of mass, the whole arrangement is referred to as a *multiple system*. While most of the stars in the night sky might appear to be single stars, at least half are actually one of these systems [4]. Out of this massive se-

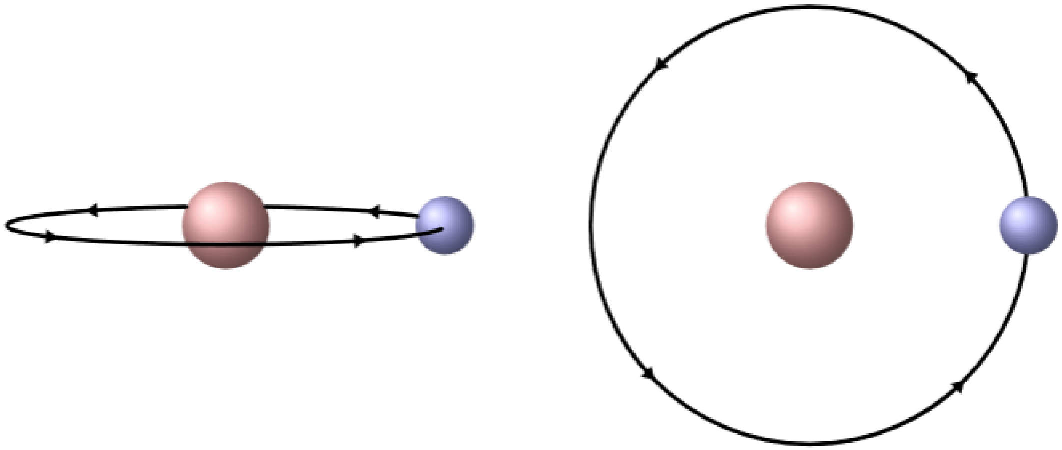

Figure 5: Cartoon representation of a two binary star systems as seen from the Earth. The system on the left would display visible eclipses, as the blue secondary star passes behind and then in front of the red primary star along its orbit. The system on the right would not produce eclipses.

lection of multiple systems, some have orbits that are angled such that component stars periodically pass in front of each other relative to the Earth, creating visible eclipses like the systems pictured in the left hand graphic of Figure 5. If such a system has only two components, this is referred to as an *eclipsing binary system*. The mathematical simplicity of the orbits involved, combined with the information that can be obtained by observing the eclipses make these systems perfect for making absolute mass and radius measurements of stars [4]. In order to make these measurements, I will define the structure and relevant variables of the system. Since all gravitational orbits take the shape of an ellipse, this requires developing a mathematical understanding of ellipses, and what observables astronomers can draw from their real-world analogs.

Once I present the language used to describe the elliptical orbits of stars in an eclipsing binary, I will derive the mathematical framework needed to derive the masses and radii of the component stars from observables that we can collect on Earth. By observing the shape and depth of the eclipses, we can draw conclusions about the inclinations of the orbit and the temperatures of the component stars. Then, by examining how the two stars affect each other's orbits, we can use Kepler's Laws to determine the mass of each component [4].

1.4.1 Fundamental Variables of Elliptical Orbits

In order to describe an ellipse, we need to define two sets of parameters. Firstly, we need to know the location of the *focii* of the ellipse (labeled F_1 and F_2 in Figure 6), and then the *semimajor* and *semiminor* axes (labeled a and b). The focii of an ellipse are the points for which the perimeter of a triangle connecting any point on the ellipse and two other points is constant, regardless of what point is chosen on the ellipse. In Figure 6, such a triangle is shown in purple. Next, we need to know the size of the ellipse, which we describe with the semimajor and semiminor axes. These distances are measured from the center of the ellipse, to the top or edge of the ellipse respectively. In the case of a binary system, the semimajor axis is always equal to the orbital separation between the two component stars.

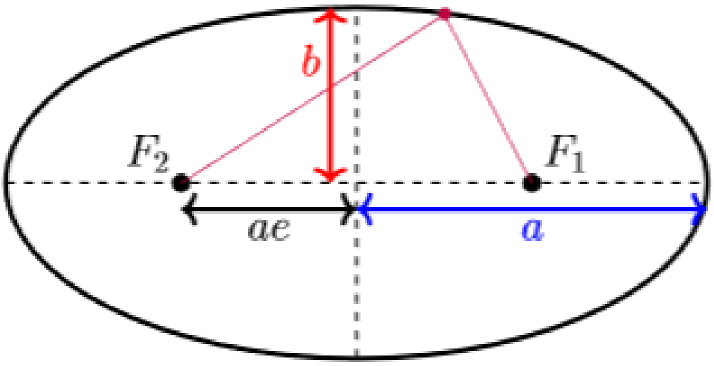

Figure 6: Diagram of an ellipse. The semimajor and minor axes are labeled as a and b respectively, and the eccentricity is given as e. The two black dots are the focii of this ellipse. The two purple lines will, for any point on the ellipse, always sum to the same length.

The semimajor axis allows us to calculate the *eccentricity* of an ellipse, which is loosely a measurement of how squished the ellipse is. Specifically, the eccentricity (typically denoted with e) is a measurement of how far the focii are from the center of the ellipse, as seen in Figure 6. An ellipse with an eccentricity of 0 is a circle, and an ellipse with an eccentricity of 1 is a parabolic orbit.

The last piece to defining an ellipse is describing how tilted it is, or its *inclination* (denoted with i). The systems shown in Figure 5 differ only in inclination: the system on the left has an inclination close to $90°$, while the system on the right has an inclination of $0°$. The inclination is measured as the angle between the semiminor axis and the plane of the sky, and is displayed graphically in Figure 7.

With these parameters to describe an ellipse, we can calculate other useful properties, like the area of an ellipse, which is given as

$$A = \pi ab, \tag{2}$$

where a and b are the semimajor and minor axes, and A is the area.

Figure 7: Side view (left) and three-dimensional visualization (right) of the relationship between orbital inclination and radial velocity. The circular orbit, shown in gray in the right image, is inclined by i degrees from the plane of the sky.

1.4.2 Radii and Temperatures From Eclipses

With this structure for understanding ellipses, we can begin to investigate how elliptical orbits can form eclipsing binary systems, and then describe what we can learn from various observables. First of all, we can parameterize what binary systems will exhibit eclipses, and which will not. Whether a binary system produces eclipses that are visible from the Earth is dependent on three factors: the inclination of the orbit (i, the orbital separation (a), and the radii of the primary (R_1) and secondary stars (R_2). Specifically, if

$$\frac{R_1 + R_2}{a} < \cos i, \tag{3}$$

then the eclipse will be visible from the Earth. In other words, the inclination of the orbit needs to be sufficiently close to 90° to cause the radii of the stars to overlap when observed from Earth. If the inclination of the orbit is 0°, then an astronomer looking through a telescope with perfect resolving power would be able to see the entirety of both stars at all times, and would never be able to see the stars cross.

Another key factor to consider is the *orbital period* of the eclipsing system. This is the amount of time that is elapsed between two identical points in a cyclical orbit, usually referred to as P. The period is extremely important to making an eclipsing system observable as such: if the period is very long, then astronomers would need to spend a lot of time observing that star to collect any useful data [4]. While there are an increasing number of surveys dedicated to finding these long-period variabilities in stars, generally speaking, the longer the period, the less likely it is for an astronomer to recognize a system as an eclipsing binary [4].

While directly watching two stars pass in front of each other would make determinations of the masses and radii of those stars fairly straightforward, this is generally not possible. Eclipsing systems are generally far enough away that a telescope would need to be prohibitively large in order to resolve the independent stars, hence the importance of the eclipses. These events take the form of periodic changes in the brightness of the target star system.

Measuring the change in brightness of a star over time, also called a *light curve*, is particularly important to making determinations of the radii of the stars. Figure 8 shows a simulated light curve from an eclipsing binary, with the two characteristic dips in brightness. The deeper dip occurs when the dimmer, cooler secondary star passes in front of

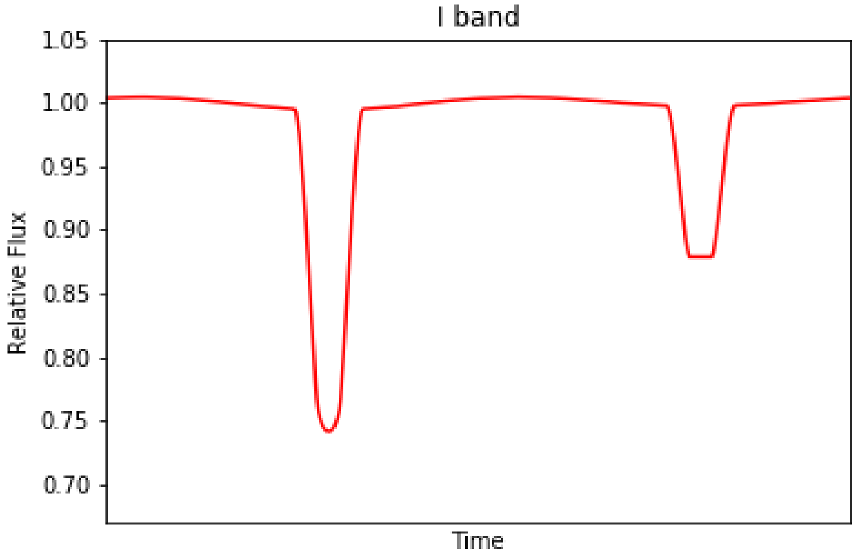

Figure 8: Simulated light curve (made with PHOEBE 2.1) for an eclipsing binary (the same system as in Figure 11). Note the deep primary eclipse (left) and shallow secondary eclipse (right). The y-axis is a unit-less measurement of the relative brightness of the star over time, referred to as relative flux.

the brighter, hotter primary star, and is called the primary eclipse. The secondary eclipse occurs when the primary star passes in front of the secondary star. The primary eclipse is deeper than the secondary eclipse because of the difference in radiance of the two stars: the primary star emits more light per unit of surface area, so when a circle the size of the secondary star is eclipsed, the amount of light blocked out is greater than the amount of light is blocked during the secondary eclipses [4]. There is no scientific distinction between which star in a binary system is designated as the primary or secondary. Rather, by convention, the brighter star is referred to as the primary star [4].

The eclipses offer astronomers a few pieces of information about the binary system, including the inclination of the orbit, the ratio of the temperatures of the component stars [4], and their radii relative to the orbital separation. The estimation of the inclination is the most straightforward: by carefully examining the shape and depth of eclipses, astronomers can determine the inclination i of an orbit [4]. If the bottom of the eclipses are flat, that implies that the inclination is very close to $90°$, as the secondary star must be completely eclipsed for some portion of the eclipse. If the eclipses are V-shaped, then the inclination is likely further away from $90°$.

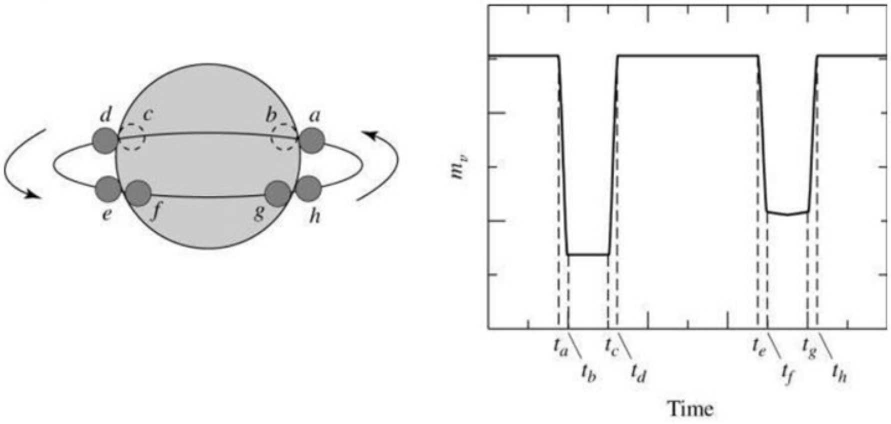

Figure 9: Diagram of important times during eclipses of a binary star. The picture on the left offers a visualization of what is happening at each time. Image Source: *Introduction to Modern Astrophysics*, Carroll and Ostlie.

The most useful piece of information that can be drawn from eclipses is the radii of both stars. If we know the radial velocities of the stars, then there is a simple kinematic solution to determining the radii. By measuring the time between the smaller star disappearing behind the larger one (times t_a and t_b in Figure 9), and multiplying that by the relative velocity of the two stars (that is, how fast the stars are moving in parallel to the observational plane), we get twice the radius of the smaller star. Expressed mathematically,

$$r_s = \frac{1}{2} v \, (t_b - t_a), \tag{4}$$

where r_s is the radius of the smaller star, $v = v_1 + v_2$ is the velocity of the stars relative to each other, and the times are the ones shown in Figure 9. We can also easily determine the radius of the larger star by measuring how long the edge of the smaller star is obscured behind the larger one. This is expressed mathematically as

$$r_l = \frac{1}{2} v \, (t_c - t_a). \tag{5}$$

Using Equations 4 and 5, along with spectra, astronomers can measure the radius of both stars in an eclipsing binary [4].

The final piece of information that can be determined from the eclipses is the effective temperature of both stars. Through an analysis of the areas of both stars and the Stefan-Boltzmann law, it can be determined that

$$\frac{B_0 - B_p}{B_0 - Bs} = \left(\frac{T_s}{T_p}\right)^4, \tag{6}$$

where B_0 is the bolometric luminosity out-of-eclipse, and B_p and B_s are the bolometric luminosities of the primary and secondary eclipses respectively (this equation is derived from first principles in *An Introduction to Modern Astrophysics*). In other words, this equation relates the relative depth of the primary and secondary eclipses to the ratio of the effective temperatures of the two stars. If this information is calculated across several passbands, an exact temperature determination can be made [14].

These three properties (inclination, radius, and temperature) are the main measurements that we can take away from just the eclipses. However, with the addition of some other types of data, we can derive more properties of the stars, like each of their masses.

1.4.3 Masses from Spectra and Radial Velocities

In addition to the eclipses themselves, eclipsing binaries provide information about the *radial velocity* of each component star by way of their spectra. Radial velocity refers to the velocity of an object towards or away from an observer, as seen in Figure 10 [4]. As the stars move around their orbit, their velocity relative to the Earth (the radial velocity, in this case) will change. Based off of the diagram in Figure 7, we can see that the radial velocity for a circular orbit is a projection of the true velocity through the angle i:

$$\mathbf{v} = \frac{\mathbf{v}_r}{\sin i}, \tag{7}$$

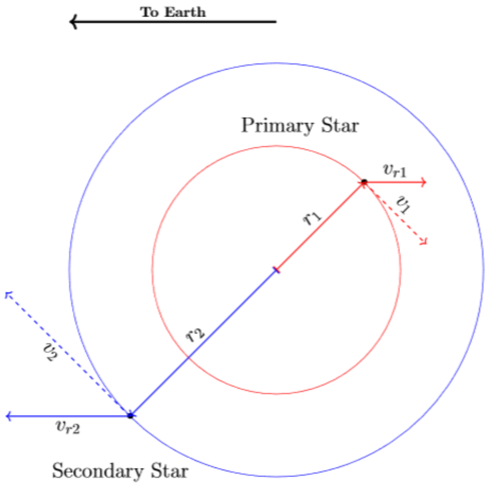

Figure 10: Example of a binary star system with circular orbits. The heavier primary star (red) has a smaller orbital radius (r_1), and a smaller radial velocity (r_{r1}) than the less massive secondary star.

where $\mathbf{v}$ is the total velocity and $\mathbf{v}_r$ is the radial velocity with respect to the observer [4]. Since the stars are moving in an orbit, the radial velocities will take the form of a ellipse projected onto one axis over time: a sinusoidal curve, like the example seen in Figure 11. As the inclination approaches $0°$, we can see that the radial velocities approach 0. However, if we are observing eclipses, then we are already guaranteed to have an inclination sufficiently large to give us meaningful radial velocities.

While perhaps there is a visual binary in the sky that moves quickly enough for astronomers to measure velocity by imaging the stars directly, the far more common (and efficient) method is to use spectra from the stars. By collecting spectra from the binary at various points throughout its period and determining their Doppler shift, astronomers can determine the velocity of the stars. The Doppler shift is defined as,

$$\frac{\Delta\lambda}{\lambda_0} = \frac{v_r}{c}, \tag{8}$$

where $\Delta\lambda$ is the difference in wavelength between some spectral feature in a target spectrum, λ_0 is the wavelength of that spectral feature at rest, c is the speed of light, and v_r is

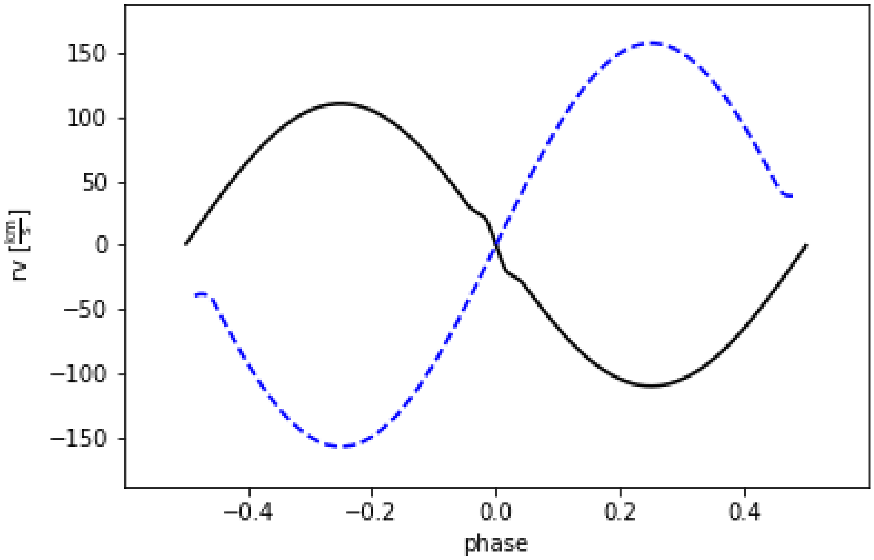

Figure 11: Simulated radial velocity curves for an eclipsing binary, made with PHOEBE 2.1. The blue dashed line represents the radial velocity of the lighter secondary star (v_{2r}), which will move faster than the heavier primary star, whose radial velocity (v_{1r}) is shown in black.

the radial velocity. This equation can be rearranged to give us the radial velocity:

$$v_r = \frac{\Delta\lambda\, c}{\lambda_0}. \tag{9}$$

In order to determine the Doppler shift of a given spectra, astronomers must have some reference point (λ_0 in Equations 8 and 9) to compare to [4]. These reference points can come from a variety of sources.

The simplest reference points take the form of specific absorption lines from stellar spectra. Each absorption line is created by atomic energy transitions for specific elements in specific energy levels. For example, hydrogen emits strongly at 6562 Å, forming a spectral line referred to as the Hα line. These absorption lines can be created in a laboratory environment, which allows researchers to get very precise measurements for each line's wavelength. By comparing the wavelength that a specific stellar spectral feature, such as the Hα line, to what is measured in a lab, a radial velocity can be calculated [3]. However, this method fails to utilize the entire range and resolution of spectra that astronomers can collect. A more comprehensive approach is to compare spectra of a target to an entire theoretical spectrum for a star of that temperature. Using this method, every piece of the spectrum contributes to the signal-to-noise ratio, instead of just the region around specific spectral lines.

Notably, this method relies on the thoroughness and accuracy of the theoretical spectrum being used. Instead, astronomers sometimes use so-called *spectral standards*. These are stars of various spectral types that have had their radial velocities carefully determined through a theoretical comparison. By using a convolution function to compare the spectra of both a target and a standard, researchers can determine how shifted a new spectrum is. The upside of using a real-life star for comparison is that there won't be any incorrect theoretical assumptions, which increases the signal that can be gained during convolution. However, the downside is that there is now noise from both the new target's spectrum and the standard's, which can negatively impact the signal-to-noise ratio. It is up to a researcher to determine which of these methods is ideal for a given situation.

Once the radial velocities of a binary system have been measured, it is a comparatively simple task to determine the masses of the component stars using Kepler's Laws [4]. Specifically, Kepler's Third Law is an invaluable tool for astronomers to determine the masses of celestial objects. Stated mathematically, the third law states

$$P^2 = \frac{4\pi^2 a^3}{G(m_1 + m_2)}, \tag{10}$$

where P is the orbital period, a is the semimajor axis, m_1 and m_2 are the masses of the orbiting objects, and G is Newton's Gravitation Constants. This equation provides two crucial insights: there is a directly calculable relationship between the orbital period and the semimajor axis, and perhaps more importantly, there is an inverse relationship between the square of the orbital period and the total mass of the system. This mathematical relationship is critical to the analysis of eclipsing binaries [14, 4].

In order to derive Kepler's Third Law, we must start with his first, which states that all bound orbits follow the path of an ellipse [27]. Through a Lagrangian analysis of two objects in bound orbits subject only to a gravitational potential, it is possible for one to derive the angular momentum, L, of such a system:

$$L = \left(\frac{m_1 m_2}{m_1 + m_2}\right)\sqrt{Ga(1-e^2)(m_1 + m_2)}, \tag{11}$$

where G is Newton's Gravity Constant, a is the sum of the semimajor axes of the two masses, and e is the eccentricity of the orbit, as derived in John Taylor's *Classical Mechanics* [27].

Consider a system with two point masses subject to no external forces. Both masses will experience a gravitational attraction towards each other in the form a *central force*, or one that always points towards the center of mass of the system. The center of mass can be thought of the weighted average of the positions of all the masses in a system. In the case of several point masses, it can be defined as

$$\mathbf{O} = \frac{\sum_i m_i \mathbf{r}_i}{\sum_i m_i}, \tag{12}$$

where $\mathbf{O}$ is the location of the center of mass relative to an arbitrary origin, $\mathbf{r}_i$ is the location of the i$^{\text{th}}$ mass to the origin, and m_i is the mass of the i$^{\text{th}}$ mass. In the case of a binary system, this takes the form

$$\mathbf{O}_{binary} = \frac{m_1 \mathbf{r}_1 + m_2 \mathbf{r}_2}{m_1 + m_2}, \tag{13}$$

where, as indicated before, m_1 refers to the mass of the primary star, m_2 refers to the mass of the secondary star, and $\mathbf{r}_1$ and $\mathbf{r}_2$ are their locations. We can define the vector $\mathbf{r}$ to be $\mathbf{r}_1 - \mathbf{r}_2$, or the vector that connects the two masses. We can now define the location of both masses in terms of the location of the center of mass (**O**), **r**, and the masses of the particle:

$$\mathbf{r}_1 = \mathbf{O} + \frac{m_2}{m_1 + m_2}\mathbf{r} \tag{14}$$

and

$$\mathbf{r}_2 = \mathbf{O} - \frac{m_1}{m_1 + m_2}\mathbf{r}. \tag{15}$$

We can see that, because both angular momentum and energy are conserved, there is an inertial reference frame in which the center of mass does not move. We know this because if there wasn't such a frame, then the center of mass would need to be accelerating. This would in turn mean that either both masses were accelerating in some direction away from the center of mass (which in turn would mean this is not a system with only a central force), or one of the masses was applying an unbalanced force to the center of mass, which would violate Newton's Third Law of Motion. This inertial frame is like any other: angular momentum and total energy are both conserved. This makes the center of mass an obvious choice for the origin of a new reference frame. When viewed in this frame, one can demonstrate that both masses will orbit around the center of mass in an ellipse, which is demonstrated in Kepler's First Law (this derivation is done most simply by solving the Euler-Lagrange Equations of Motion, which is shown in full in John R. Taylor's *Classical Mechanics* [27]).

With our origin selected to be the center of mass, we can begin to work towards Kepler's Third Law. Consider the simple orbit shown in Figure 12, which shows the orbit of a point mass around a center of mass, O. We can define **r**, or $\overline{OP}$, to be the distance of the mass from the origin, and **v** to be the mass's velocity. If **r** starts at point P and moves to Q, then it will sweep over the shaded area labeled dA. We can approximate the arc between P and Q to be the straight path

$$\overline{PQ} = d\mathbf{r} = \mathbf{v} \cdot dt, \tag{16}$$

since over the infinitesimal time t, this is the case. Recalling that the area, A, of a triangle

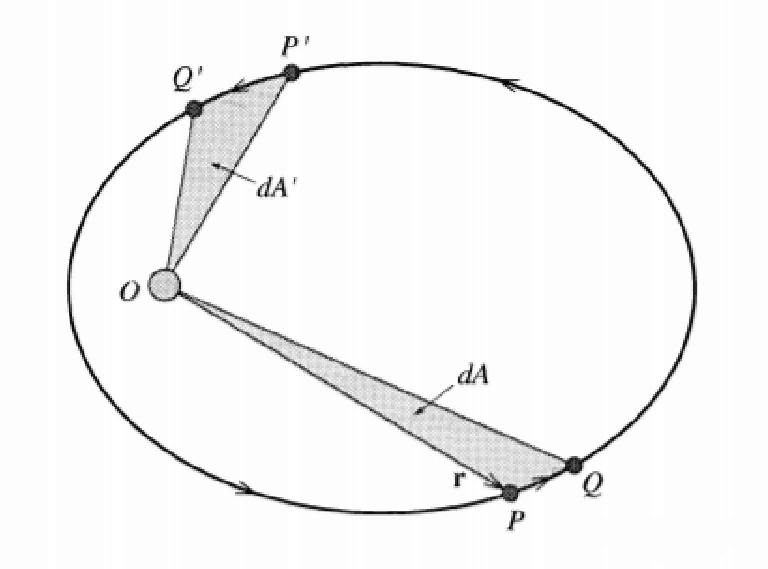

Figure 12: Diagram of the orbit of a point mass around the origin O. Image adapted from Figure 3.7 in *Classical Mechanics* by John Taylor [27].

defined by adjacent vectors **r** and **b** is

$$A = \frac{1}{2}|\mathbf{a} \times \mathbf{b}| = \frac{1}{2}|\overline{OP} \times \overline{PQ}|, \tag{17}$$

we can see that

$$\frac{dA}{dt} = \frac{1}{2}|\mathbf{r} \times \mathbf{v}dt|. \tag{18}$$

We know that the momentum of our mass is $\mathbf{p} = m \cdot \mathbf{v}$, which we can plug into the above to arrive at

$$\frac{dA}{dt} = \frac{1}{2m}|\mathbf{r} \times \mathbf{p}|. \tag{19}$$

Next, we can see that we have $\mathbf{r} \times \mathbf{p}$, which is the definition of the angular momentum, l of our particle. This allows us to make our equation into

$$\begin{aligned} \frac{dA}{dt} &= \frac{|\mathbf{l}|}{2m} \\ &= \frac{L}{2m}, \end{aligned} \tag{20}$$

where L is the magnitude of the angular momentum. This tells us that the area swept over by **r** over time t ($\frac{dA}{dt}$) is equal to a constant, since L is, by the conservation of angular momentum, by definition constant. This is Kepler's Second Law, which states that as an object orbits around a fixed origin, it sweeps over equal areas in equal times. We can generalize this equation to two masses orbiting about a fixed center of mass by replacing the mass of our particle, m, with the reduced mass of the system,

$$\mu = \frac{m_1 m_2}{m_1 + m_2}, \tag{21}$$

where m_1 and m_2 are the masses of the two point masses. The reduced mass comes from using Equations 14 and 15 to define the kinetic energy, T, of the system:

$$\begin{aligned} T &= \frac{1}{2}m_1\left(\frac{d\mathbf{r}_1}{dt}\right)^2 + \frac{1}{2}m_2\left(\frac{d\mathbf{r}_2}{dt}\right)^2 \\ &= \frac{1}{2}\left[m_1\left(\frac{m_2}{m_1+m_2}\frac{d\mathbf{r}}{dt}\right)^2 + m_2\left(-\frac{m_1}{m_1+m_2}\frac{d\mathbf{r}}{dt}\right)^2\right] \\ &= \frac{1}{2}\left(\frac{m_1 m_2}{m_1+m_2}\right)\frac{d\mathbf{r}}{dt}^2 \\ &= \frac{1}{2}\mu\frac{d\mathbf{r}}{dt}^2 . \end{aligned} \tag{22}$$

Here, we can see that in a frame where the center of mass is stationary, the total kinetic energy of the system can be phrased as the kinetic of a fictitious particle with location **r** and mass μ. This is important, because it allows us to treat the two stars and their orbits as one single particle with one orbit, greatly simplifying the math involved.

Using the reduced mass gives us Kepler's Second Law, as it applies to binary systems,

$$\frac{dA}{dt} = \frac{L}{2\mu}. \tag{23}$$

In order to derive Kepler's Third law, we need to first integrate over an entire period of one our mass's orbits, in order to get the total area within the ellipse. Mathematically, this becomes

$$\begin{aligned} A &= \int_0^P \frac{L}{2\mu} dt \\ &= \frac{L}{2\mu} P. \end{aligned} \tag{24}$$

Next, we can substitute in the equation for the area of an ellipse from Equation 2 to get

$$\begin{aligned} \pi ab &= \frac{L}{2\mu} P \\ P &= \frac{2\pi\, a\, b\, \mu}{L}. \end{aligned} \tag{25}$$

$$P^2 = \frac{4\pi^2\, a^2\, b^2\, \mu^2}{L^2} \tag{26}$$

We know the total angular momentum of the system from Equation 11, which we can substitute into Equation 26 to give us our result, Equation 10:

$$P^2 = \frac{4\pi^2 a^3}{G(m_1 + m_2)}. \tag{27}$$

In addition to Kepler's laws, there are more useful mathematical relations that fall out of the equations of motion for orbits that are useful to astronomers. Let us consider a binary orbit in which both point masses have circular orbits (not an unreasonable assumption for binary systems[1]). In this case, the velocity of each mass is constant in magnitude over time. Specifically, the velocities can be expressed as

$$\mathbf{v}_1 = \frac{2\pi r_1}{P} \tag{28}$$

and

$$\mathbf{v}_2 = \frac{2\pi r_2}{P}, \tag{29}$$

---

[1] All stars in binary orbits exert small forces on each other, referred to as *tidal forces*. Over a relatively short time, these forces circularize the orbits, and cause the stars to become tidally locked, where the same side of each star always face each other, much like the Earth and the Moon [4].

where r_1 and r_2 are the radii of the circular orbits, and P is the orbital period. Note that, although the radii can differ, the period is always the same for both orbits. We can rearrange these expressions to give us an expression for the radius of each orbit in terms of orbital period and velocity:

$$r_1 = \frac{\mathbf{v}_1 P}{2\pi} \tag{30}$$

and

$$r_2 = \frac{\mathbf{v}_2 P}{2\pi}. \tag{31}$$

Next, we can observe that, given our definition of the center of mass,

$$\frac{m_1}{m_2} = \frac{r_2}{r_1}, \tag{32}$$

which is fully derived in Carroll and Ostlie [4]. We can plug in our findings from Equations 30 and 31 to get the following:

$$\frac{m_1}{m_2} = \frac{\mathbf{v}_2}{\mathbf{v}_1}. \tag{33}$$

This relates ratio of the masses of each object in the binary system to the inverse ratio of their velocities. If we instead want to solve for the radial velocities of an inclined orbit with respect to an observer on Earth, we need only add in a $\sin i$ term (as seen in the previous section), which gets cancelled out, giving us

$$\frac{m_1}{m_2} = \frac{\mathbf{v}_{r2} \sin i}{\mathbf{v}_{r1} \sin i} = \frac{\mathbf{v}_{r2}}{\mathbf{v}_{r1}}, \tag{34}$$

where $\mathbf{v}_{r1}$ and $\mathbf{v}_{r2}$ are the radial velocities of the primary and secondary stars respectively. In other words, the ratio of the radial velocities is constant, and is always inversely proportional to the mass ratio of the system at any time and location in the orbit.

In order to determine masses (as opposed to the mass ratio) from the radial velocities and period, a few more pieces are needed. If we define a as the sum of the semi-major axes of both orbits (i.e. $a = r_1 + r_2$), we see that

$$a = r_1 + r_2 = \frac{\mathbf{v}_1 P}{2\pi} + \frac{\mathbf{v}_2 P}{2\pi}, \tag{35}$$

from Equations 30 and 31. We can plug this into Equation 10 and solve for the sum of the masses, which gives us

$$m_1 + m_2 = \frac{P}{2\,\pi\,G}\left(\frac{(v_{1r} + v_{2r})}{\sin i}\right)^3, \tag{36}$$

where v_{1r} and v_{2r} are the radial velocities, and i is the inclination. This equation tells us that, if we know the radial velocities of both stars and the inclination, we can calculate exactly the total mass of the binary system. By combining this with Equation 33, we can exactly calculate the masses of both stars. This result is precisely why eclipsing binaries (as opposed to simple visual binaries) are so important to astronomy: the inclination can be measured along with the radial velocity, giving exact mass measurements.

However, it is not always guaranteed that both radial velocities can be determined, as is the case with the subject of this report, MML 48. This can occur because the secondary star is dim enough that its spectra is overwhelmed by the noise from the primary's spectra. In the case where only one radial velocity is measurable, we can replace the radial velocity of one of the stars with the ratio of the masses, giving us

$$m_1 + m_2 = \frac{P}{2\,\pi\,G}\left(\frac{v_{1r}}{\sin i}\right)^3\left(1 + \frac{m_1}{m_2}\right)^3, \tag{37}$$

which can be rewritten as the so called mass-function:

$$\frac{m_2^3 \sin^3 i}{(m_1 + m_2)^2} = \frac{P v_{1r}^3}{2\,\pi\,G}. \tag{38}$$

Note that the right side of the equation contains only easily measured values (the radial velocity of one star and the period). While this equation cannot give definite values of mass (as we cannot utilize Equation 33), it does provide limits on the values for the masses and inclination that can be used to conduct statistical analyses.

1.5 Modeling of Eclipsing Binaries with PHOEBE 2.1

While determining the mass and radii of component stars in eclipsing binaries is extremely useful, modern computing allows astronomers to determine far more properties of stars through the use of advanced modeling [4]. Using a model-driven approach, researchers construct a simulated model of a system and iterate it to match observed data, rather than try to conduct measurements directly on data. There are several different programs that enable the creation of these simulated systems, but this project focused on the use of PHOEBE 2.1, a python library that enables its users to generate artificial light curves and radial velocities for arbitrary eclipsing binary systems.

Fundamentally, all versions of PHOEBE are libraries of code that solve Kepler's laws for an arbitrary system [24]. PHOEBE adds to this simple functionality by computing theoretical observables like radial velocities and light curves that an astronomer could measure from the Earth. These theoretical observables also include distortions from Kepler's laws caused by a large number of background factors. The benefit of using PHOEBE is that it handles both the orbital mechanics, and the minutia of the observables, all in one place.

1.5.1 Background on PHOEBE

PHOEBE 2.1 is the second generation of the PHOEBE modeling program. PHOEBE 1.0, now referred to as the legacy version of PHOEBE, was published in 2005 as an extension of the existing Wilson and Devinney eclipsing binary modeling program [24]. In 2016, to meet the demands for high precision modeling, PHOEBE 2.1 was released, resting on a rewrite of the Wilson-Devinney code-base. Specifically, the level of detail available from the numerous space telescopes and large telescopes on the ground were detecting levels of detail that revealed phenomena that had previously been hidden in noise, such as surface reflectively, gravity darkening, and limb darkening [23].

Modeling with PHOEBE 2.1 begins with a default eclipsing binary, which when computed, simulates a binary system with two solar mass stars orbiting each other. The user can input new stellar parameters, ranging from obvious parameters such as mass ratio, radii, orbital period, or effective temperature, to more obscured parameters such as atmosphere models, limb darkening functions, and surface reflectively. Once a desired set of stellar parameters has been selected, PHOEBE 2.1 can generate simulated light curves, radial velocities, and line profiles of the system as it would be seen from Earth, in addition to other useful visualizations of the system [23]. Researchers can compare the model's output with their own data, and then use the residuals to tweak the model until they agree. The method by which a model is iterated is entirely up the the user: PHOEBE 2.1 does not have a built in optimizer.

1.5.2 Effect of Different Parameters on Observables

PHOEBE 2.1, while primarily designed for modeling specific eclipsing binary systems, can also be used to generate models of systems for visualization purposes. In this section, I will demonstrate the impacts of certain stellar parameters on the light curves that would be collected from such a system.

First, we can examine the impact of various inclinations on the light curves that one might observe. In Section As shown in Figure 13, as the inclination gets lower, there are two key effects: the depth of the eclipse goes down (which makes sense: less of the smaller star is blocked out by the larger one), and the shape of the eclipses gets less flat and more U shaped. Additionally, the relative depth of the eclipses is independent of the inclination, and the width of the eclipses does not vary significantly.

Next, we can examine the impact of the ratio of radii on the light curves. Figure 14 shows the impact of the secondary star being made smaller. As we can see, both the width

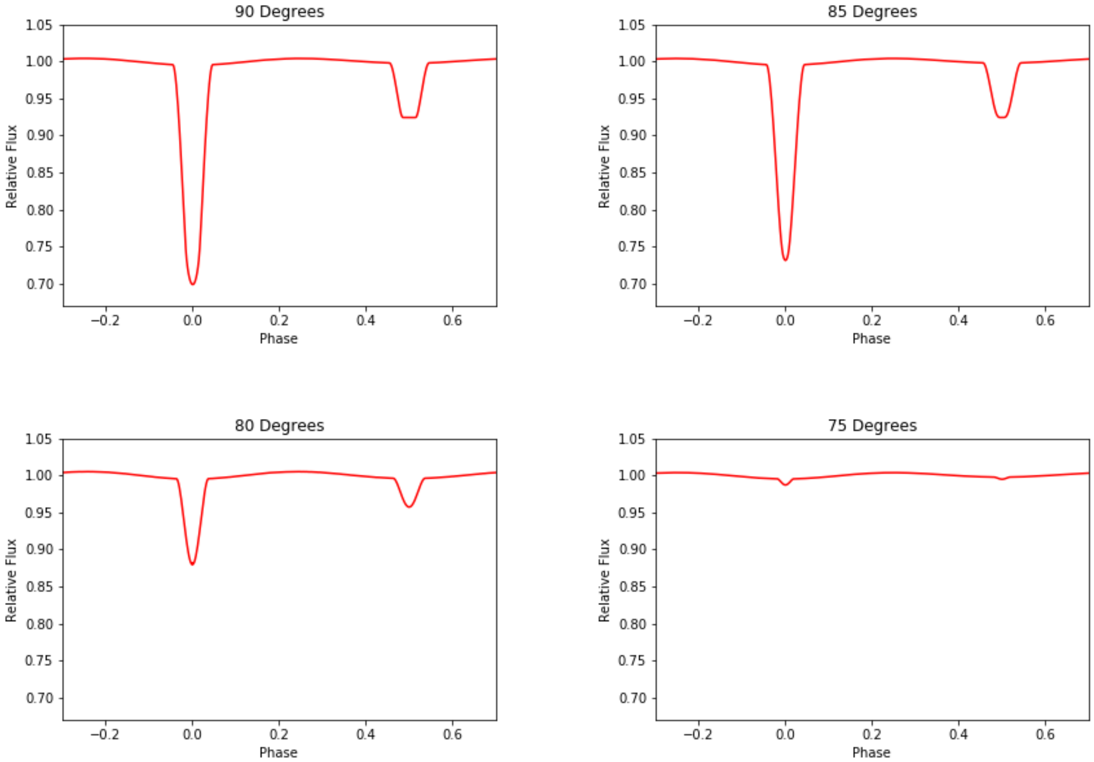

Figure 13: Simulated light curves for an eclipsing binary system with varying inclinations. The simulated system has a primary star that is twice as large (in both mass and radius) as the secondary, and the orbits are both circular.

and depth of the eclipses changes noticeably with radius. However, the general shape (e.g. the flatness of the transit) remains roughly the same, as this is primarily determined by the inclination.

There are dozens of parameters beyond eccentricity and radii that impact the shape of the light and radial velocity curves that PHOEBE 2.1 can produce. For example, PHOEBE incorporates the masses, effective temperatures, eccentricity, and many other properties into its model. There are parameters beyond the physical properties of the stars that also need to be set. Below, I provide a list and brief summary of the parameters that have noticeable impacts on the outcome of simulations:

1. Limb Darkening Function: This parameter determines how PHOEBE 2.1 calculates the radiance of each section of a star. Since light from the edge of the star has to pass

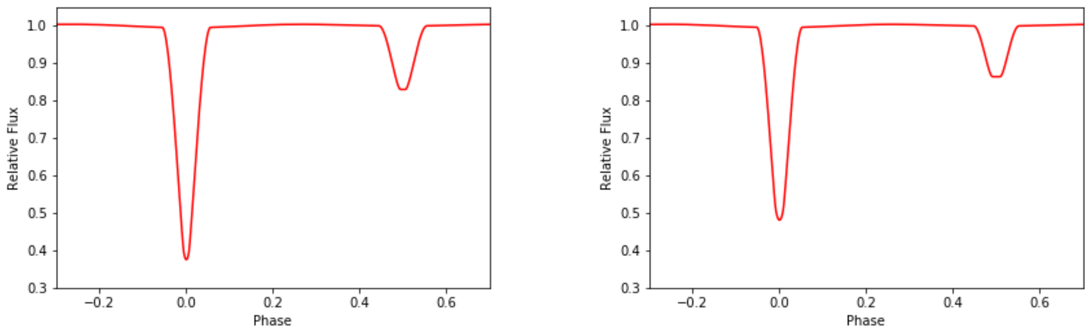

Radius Ratio = .80 $R_\odot$

Radius Ratio = .70 $R_\odot$

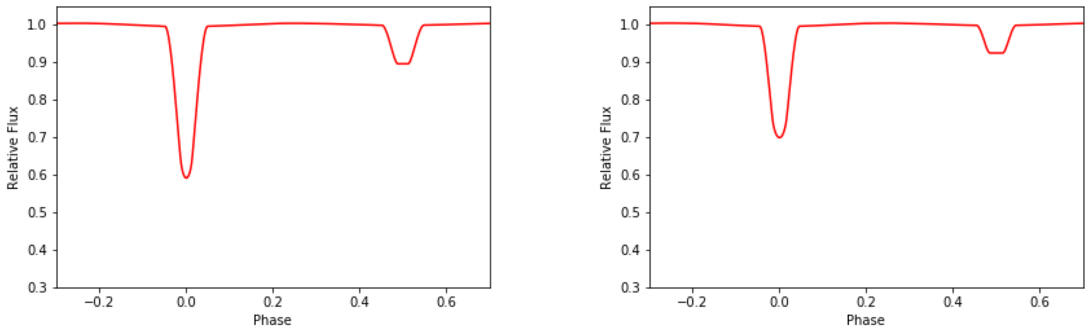

Radius Ratio = .60 $R_\odot$

Radius Ratio = .50 $R_\odot$

Figure 14: Simulated light curves for an eclipsing binary system with varying radii. This system has the same parameters as in Figure 13, except with varying radii and an inclination of 90°.

through more stellar atmosphere to reach the Earth, the edges appear darker. This effect can be seen in Figure 15.

2. Surface Reflectively: This parameters tells PHOEBE 2.1 how to simulate the light and heat transfer between the two stars in the binary. As light radiates from one star, some of it will hit the other and cause some combination of localized heating and reflection. This parameter controls how much incoming light is reflected.

3. Stellar Atmosphere Models: The light that is emitted from a star has to pass through that star's atmosphere. The exact way that light interacts with different layers of the atmosphere is not known, but several different models provide ways to calculate how it might happen. PHOEBE 2.1 supports several different pre-computed stellar atmosphere tables, which can impact how the simulated light curves appear. PHOEBE

2.1 can also treat stars as an ideal blackbody radiator instead of using an atmosphere model.

4. Passbands: When PHOEBE 2.1 computes light curves, it defaults to calculating bolometric flux, or the brightness in all wavelengths. However, astronomers collect data in specific wavelength ranges, which PHOEBE needs to replicate. PHOEBE supports several dozen different passbands, including the generic Johnson/Cousin's filters, along with several different filters from space telescopes.

While this list of parameters is by no means exhaustive, it does highlight the range of different features that PHOEBE 2.1 can simulate.

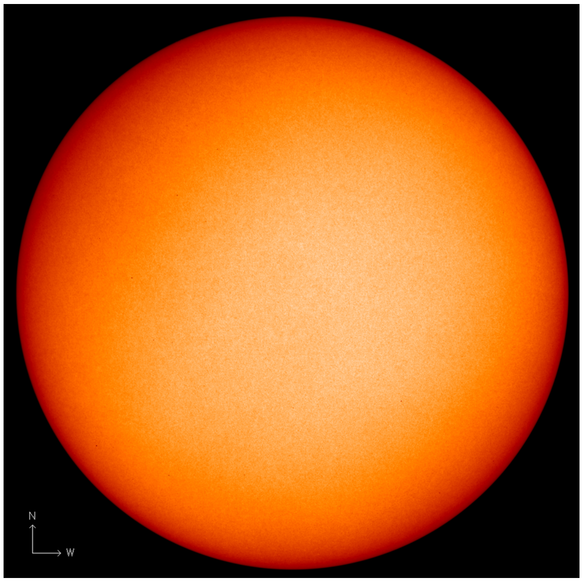

Figure 15: Image of the sun. Note that the brightness decreases around the edge. This effect is the result of limb darkening. Image Source: NASA Earth Observatory.

1.6 Background on MML 48

MML 48, the topic of this research paper, is a southern-sky object in the Upper-Centaurus Lupus subgroup of the approximately 16 ± 2 Myr old Scorpius-Centaurus OB association (RA 14:41:35.0, DEC -47:00:28.7), as seen in Figure 18 [17, 29]. MML 48's young age was initially determined through observations of its X-ray emissions, with confirmation coming from an analysis of the quantity of lithium in its atmosphere [10].

MML 48's eclipsing nature was determined through observations from the All Sky Automated Survey (ASAS) which are presented in Figures 16 and 17. MML 48 was then observed as part of the SuperWASP survey (a wide-field photometric variability survey aiming to detect transiting exoplanets around main-sequence stars). SuperWASP cameras image bright stars (with magnitudes of around 9-13) using a broad V and R-band filter, with approximately 1$\%$ accuracy. MML 48 was observed with the WASP-South telescope and instrumentation [21] in the spring observing season from 2006-2008 and again from 2011-2014 [10]. An analysis of the SuperWASP data determined the Heliocentric Julian Date for a primary eclipse to be $2454945.0394 \pm 1 \times 10^{-4}$, with an orbital period of $2.0171078 \pm 2 \times 10^{-7}$ days.

Filter	Magnitude	Error
B	10.79	0.04
V	9.986	0.067
I	8.959	0.041
G	9.7787	0.0020
J	8.465	0.024
H	8.005	0.040
K	7.901	0.020

Table 1: Magnitudes for MML 48 in various filters. The data collected for this project utilized the B, V, I, and R (not listed above) filters. (Sources: B [12], VI [16], G [9], JHK [6]).

MML 48 has been measured to be 373 ± 4 ly away from Earth via GAIA parallax measurements [19]. Fluxes for MML 48 were collected in 2012, are are presented in Table 1.

The data collected above demonstrates why MML 48 presents an enticing observational target for researchers. As an eclipsing binary, it provides researchers a direct way of calculating the masses and radii of each component star, and evidence from the star's makeup

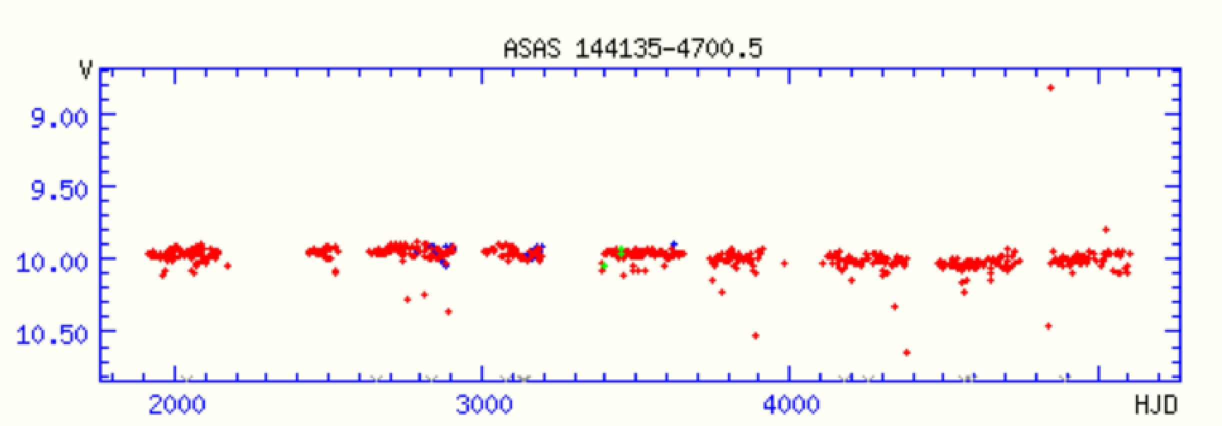

Figure 16: Light curve collected by ASAS-3. This figure was generated directly from the ASAS web portal (*http://www.astrouw.edu.pl/asas/?page=aasc*). The eclipsing nature of MML 48 is not readily apparent, but once phase folded (as shown in Figure 17), it is much clearer. Phase-folding refers to the process of plotting data from an eclipsing binary with the orbital phase on the x-axis instead of the absolute date, which allows repeated behaviors to be seen.

and locality indicate that the system is a young, pre-main sequence star. This combination of features is rare amongst observed stars: as of 2019, only 14 other pre-main sequence eclipsing binaries have been fully analyzed. The list of these binaries is given in Chew et. al and the references therein [10]. Additionally, MML 48's period is close to exactly two days, so eclipses can be readily observed on consecutive nights [16]. All of these factors explain why we chose to observe MML 48.

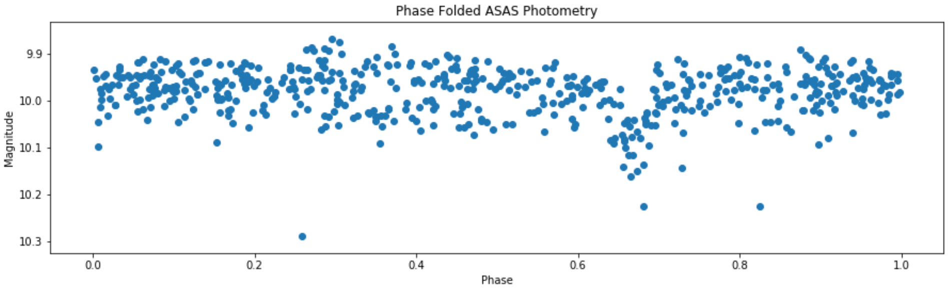

Figure 17: Phase folded light curve generated from the raw ASAS data. Outlying points (magnitude greater than 10.3 and less than 9.8) were not plotted to make the primary eclipse (phase 0.65) visible. The data was not well enough resolved to observe the secondary eclipses.

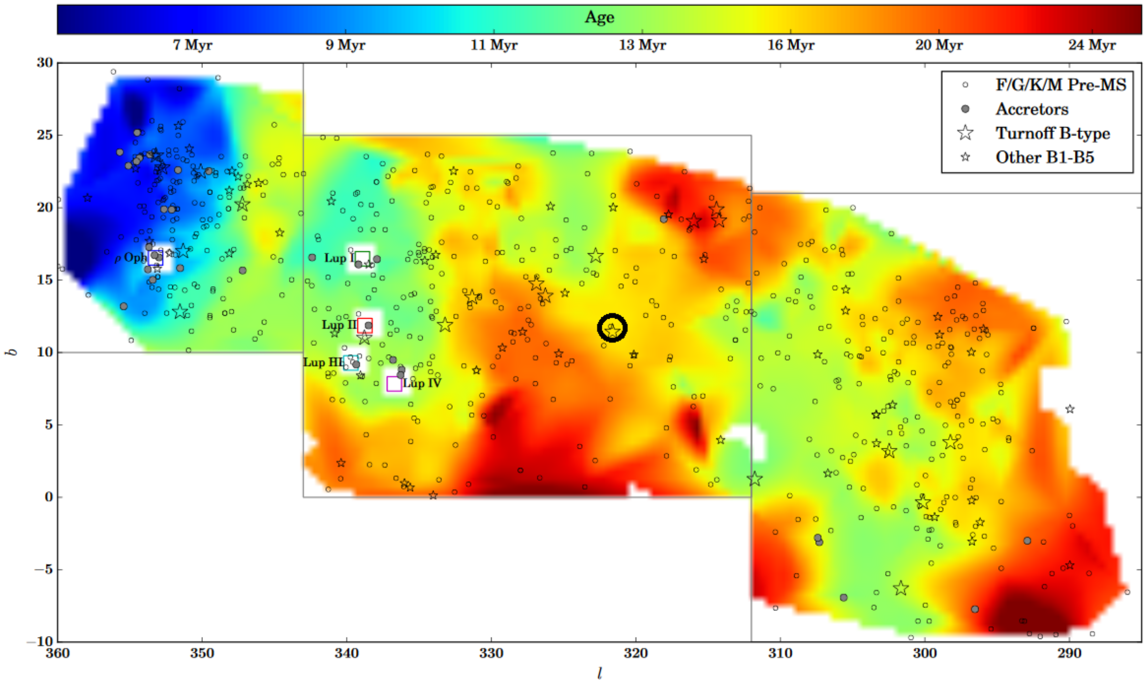

Figure 18: Location of MML 48 in the Upper-Centaurus Lupus Star Forming Region. MML 48 is the partially obscured F/G/K/M Pre-MS star in the center of the black circle. The axes are given in galactic coordinates. Figure adapted from Pecaut and Mamajek, 2016 [20].

2 Data Collection

While the observations confirming the age and eclipsing properties of MML 48 are interesting, they do not provide the most useful pieces of information that an eclipsing binary can provide: the masses, radii, and temperatures of the component stars. As explained in the introduction, high resolution spectrography is required to measure the radial velocities that yield mass, and multi-band photometry is required to measure the effective temperature and radius of the stars. The ASAS and SuperWASP photometry were both insufficiently resolved to observe the secondary eclipses, and both were collected in only one filter (as is typical in all-sky surveys).

This lack of sufficient data was the driving purpose behind my observing run in March. In order to collect the time-series photometry, I utilized a 0.9 meter telescope at the Cerro-Tololo Inter-American Observatory (CTIO) 50 miles east of La Serena, Chile. This telescope suited my needs very well. Firstly, MML 48 is in the southern sky, so I needed a telescope in the southern hemisphere. Secondly, since MML 48 is a bright target, I did not need to use an extremely large telescope in order to make meaningful observations. Next, this telescope has a fairly wide field of view (13'x13', or roughly 46% of the full moon), which meant that my science images would have a large number of bright reference stars [1]. Thirdly, the 0.9 meter telescope is cryogenically cooled, which enables high precision measurements (this is explained further in the following section). Finally, the dates were selected to allow for several consecutive nights of observable eclipses. By a stroke of luck, those nights also overlapped with spring break at HWS, which facilitated my ability to collect my data.

The only downside of using the 0.9m CTIO telescope was the age of the CCD. The telescope is primarily used in a long-term sky survey, and so its detector has not been updated since 2000 [1]. While the quality of the images is not impacted by this, the readout time for the detector (which is the bulk of the time between each exposure) was around 30 seconds. While this might not seem that bad, over the course of the night, this added up to more than a full hour of readout time. However, this downside was easily outweighed by the upsides. For these reasons, we applied for and were awarded observing time at this telescope for the observation of MML 48.

2.1 Images and Calibrations Needed for Astronomical Photometry

In order to make meaningful measurements from images taken with a telescope and detector, we needed a few types of images: the images of the target, and images to calibrate those scientific images. All images from a CCD detector (such as the one we used) take the form of a 2D array, where each value stores a number that is directly correlated to the number of photons that struck the detector in that pixel during an exposure.

The main source of data is from *science images*, or the images of the target being studied. An example science image can be seen in the right picture in Figure 19. The number of

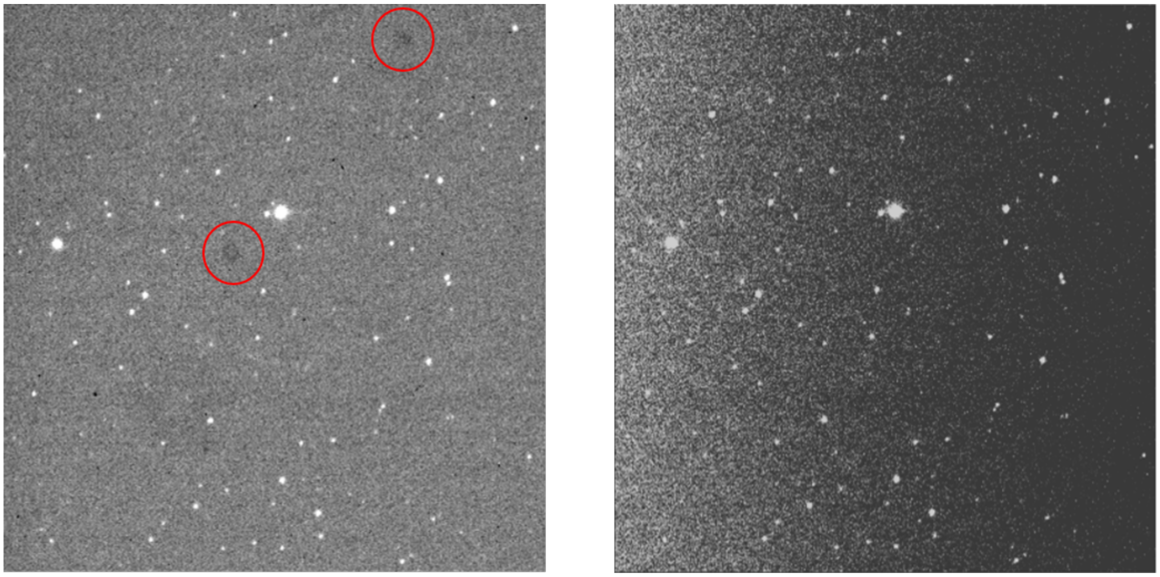

Figure 19: Science image before (left) and after (right) flat-fielding. The image on the left has noticeable dark spots from dust in the telescope/detector. After the flat field image is used to calibrate the image, the dark spots disappear. The gradient present in the right image is an artifact of the scaling of the image: the lighter-left side is only around 20 counts brighter than the right side, which is insignificant compared to the roughly 30,000 counts of our target.

counts in the region covered by a target can be compared to other stars in the region to give some quantitative measurement of the brightness of the target, which is the primary goal of time series photometry. The other images are all taken in order to calibrate these science images. Specifically, there are three main sources of irregularity that need to be accounted for [3].

Firstly, the CCD used to collect each image is able pick up its own latent heat as noise [3]. This means that every pixel in an image will have measured an amount of random noise correlated to how long the exposure time was. This noise can be accounted for in two ways. Smaller telescopes will typically collect *dark images*, which are exposures of the same length as the science images, but with the aperture completely closed. This causes each pixel to measure only noise for however long it was exposed for in the science image. By subtracting the average of several dark images, the latent heat noise can be effectively mitigated [3]. The other method for handling the heat of the detector is simply to cool the detector enough that the latent heat does not induce noise in the detector [3]. Since the 0.9

meter CTIO telescope is cooled with LN_2, I did not need to collect dark images.

Secondly, every CCD will artificially inflate the number of counts in each pixel as the image reads out, which is done purposefully to prevent any pixel from ever measuring a negative value [3]. This readout error can be mitigated with a *bias image*. These images are instantaneous exposures, so each pixel value will measure only the noise from the readout process [3]. A median of several bias images need to be subtracted from every other image collected with the detector in order to fully account for the readout noise.

The final source of irregularities stems from dust and debris on the mirrors and detector, and physical defects in the silicon wafer that comprise the CCD [3]. Any particle will reduce the brightness of the image at that location, which will obviously interfere with measurements of a star's brightness. Similarly, any defect in the silicon can selectively increase or decrease the brightness of any given pixel [3]. These irregularities are accounted for with *flat field* images. These images are exposures taken of a uniformly bright field, such as the sky just after sunset, or a uniform light source. Since in theory any image of such a source should be completely uniform, and deviation from the norm can be identified [3]. By subtracting a bias image from a flat field, and then normalizing each flat field, a map of the amount of error in each pixel can be produced. By dividing each science image by this normalized flat field, those defects will disappear [3]. This can be seen clearly in Figure 19.

Collecting these images (science, bias, and flat) occupied the bulk of my time while observing.

2.2 Observation Plan

The first step in collecting data is coming up with a plan. Specifically, leading up to the observing run at the CTIO 0.9m telescope in march, we created a document that compiled all of the information an observer might need in order to effectively observe into one place. This includes basic information such as finding charts, RA/DEC, and the apparent magnitudes of the target in various bands, along with a list of nearby reference stars. Additionally, observatory-specific information is important to include, such as astronomical twilight times, target rise/set time, angular lunar separation, and other location/time specific parameters.

The table of important times is presented in Table 2. The first column gives the date at the beginning of each night observing (that is, the date of the preceding midnight). The second column gives the Local Mean Sidereal Time, which is one measurement of time used by astronomers that is based on the location of stars in the sky. The other commonly used time is Universal Coordinated Time (UTC, also called Greenwich Mean Time), which is close to the mean solar time at 0° longitude. The third column has the time of each sunset. This time is important, because the time between the sun setting and the sky becoming fully dark is the optimal time to collect flat field images. The next two columns display the evening and morning twilight, respectively. For this table, I used astronomical twilight, which refers to when the sun is 18° below the horizon, which is the time at which the sun no longer illuminates the sky [3]. Finally, the last column displays the time of the deepest part of the eclipse for each night. The secondary eclipses occurred on the nights with shaded rows.

Date	LMST at Midnight	Sunset	E. Twilight	M. Twilight	Eclipse Time
2019-03-16	06:49:55	19:56:41	21:20:46	06:23:44	01:30:40
2019-03-17	06:53:56	19:55:29	21:19:29	06:24:28	01:42:59
2019-03-18	06:57:48	19:54:17	21:18:11	06:25:11	01:55:18
2019-03-19	07:01:45	19:53:04	21:16:54	06:25:53	02:07:37
2019-03-20	07:05:41	19:51:51	21:15:37	06:26:35	02:19:56
2019-03-21	07:09:38	19:50:38	21:14:20	06:27:16	02:32:15
2019-03-22	07:13:34	19:49:25	21:13:03	06:27:56	02:44:34

Table 2: Table from the observing plan. All of the times are given in Chilean Local Time on March 11th (UTC - 4).

Next, the plan included *altitude plots* of MML 48. These are graphs that display the altitude of a target over time, and they provide an easy way to tell at a glace when a target is observable, or susceptible to lunar interference. There is one altitude plot for each night of observing, since each night was slightly different.

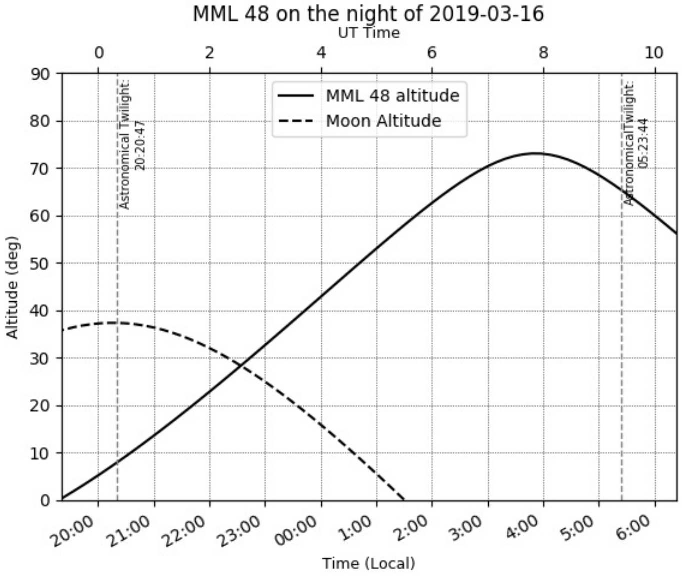

Figure 20: Sample altitude plot from the observation plan. The altitude of MML 48 is shown with the solid line, and the Moon's altitude is shown with the dotted line. Altitudes are given in degrees above the horizon. Improvements to this plot would include marking eclipse ingress/egress times, and labeling the minimum lunar angular separation.

The next section of the plan was intended to be dedicated to outlining the day-to-day plan for the observing run. Specifically, it was supposed to lay out a timeline for taking bias images and dome flats in the afternoon, setting up the telescope for observing in the evening, collecting sky flats, and then a list of science images to be obtained. However, since I hadn't been on an observing trip like this, I didn't know what to put in those sections. A more careful look at what should have been there is presented in the following section.

The final pieces of the plan I made was information about MML 48 itself: its right ascension and declination (the coordinates used to locate stars in the night sky by astronomers), fluxes in various filters, finding charts, and nearby photometric standards. This section enabled us to have ready access to the basic information we would need once we arrived at the telescope.

The plan was partially generated by a python script, and partially hand written. I wrote a script using the Python package astroplan, which provides tools for planning observing runs. My script automatically generated the table of times and altitude plots, and inserted them into a formatted LaTeX document, with empty headers for the sections to be filled in manually.

2.3 Review of March CTIO Observation Plan

This observing plan, while sufficient to get by, needs a lot of improvements. Notably, the times presented in Table 2 were not in UTC, the altitude plots were missing some useful information such as the angular separation between MML 48 and the moon, and the sections that actually constituted a daily plan were essentially empty.

First and foremost, the times presented in the graphs and tables were presented in local time. While this seems like a convenient feature, it raised a few issues. Firstly, local time is not particularly useful to locating potential targets in the sky. During our observing run, we had a few hours before our target rose to observe various targets, either for scientific or aesthetic value. We did not plan out what targets we would observe before we arrived at CTIO, and finding targets based off of local time involved more scratch-work than was ideal, and having information about the target in UTC would have enabled smoother determination of new targets. Furthermore, Daylight Savings Time occurred between the creation of the plan and the observing run. This meant that all of the local times were off by one hour. If those times were initially presented in UTC time, then no effort would have been needed to convert the times back and forth every night. Even though the conversion involving only offsetting by an hour, the whole point of the plan is to remove as much thinking from the process as possible. More to the point, basically every scientific observatory has a clock display UTC time, so presenting times in the plan in UTC would be easily deciphered by the reader anyway.

Next, the table in the plan needed more information. Based off of conditions at the observatory, astronomical twilight was probably too extreme of a cutoff for observations: because our target was bright, nautical twilight would have been a perfectly acceptable time to begin and end observing. Information about the eclipse ingress and egress times were both critical to observing and missing from the table, along with the target's rise and set times. This information is important to have with respect to selecting other targets for the night, as well as timing calibrations.

In addition to the table being incomplete, the graphs had a few flaws. Firstly, while knowing the altitude of the moon is helpful, adding information about the minimum angular separation, as well as the moon's phase, to the graphs would have been helpful for determining when that might become a problem. Secondly, the graphs should have had vertical lines with specific times labeled, such as target rise/set, eclipse ingress/egress, and moon-rise/set times. Having these values be graphically available would have been helpful. Thirdly, the graphs should simply have been larger, to enable easier and more accurate reading.

The set-up and calibrations section was also completely devoid of useful information. Retrospectively, it is easy to see what information would have been useful, but at the time of writing, I did not know where to find the information needed to fill in this section. This includes specifically what types of calibrations will be taken and at what time, rough estimates about exposure times in different filters, and a plan for what to do with the time before target rise.

Were this plan remade, I would make some fundamental changes. Firstly, I would split it into one page per night. Each page would have the relevant information for that night only: the times presented in the table (this time in UTC), along with eclipse ingress and egress times, the altitude plots, and any relevant calibration information. Even if there were elements repeated on each page, having all of the information for a night in one spot would have been helpful.

2.4 Overview of Data Collected

The observing run at the 0.9m CTIO telescope in March lasted for 8 nights. However, due to technical problems, data from the first two nights were discarded, which resulted in only collecting six nights of data. This produced a dataset of 3 primary eclipses, and 3 secondary eclipses. This section outlines the data and calibrations that were collected on these nights. A summary of the number of images of each type is presented in Table 4.

In addition to the time series photometry that we collected at the 0.9m CTIO telescope, simultaneous spectra was collected at the adjacent 1.5m CTIO telescope (connected to the CHIRON spectrograph) by Fred Walter. The spectra produced by CHIRON cover a range of 410-870nm, and take the form of several orders: small sections of whole spectra that are stacked vertically on a CCD detector by a grating in the instrument [28]. The spectra used are presented in Table 3, along with the results of the radial velocity extraction explained in Section 3.3. The combination of the photometry and spectra collected of MML 48 formed the data that was processed as part of this project.

Filename	Date (HJD)	Phase	Radial Velocity (km/s)	Error (km/s)
mml48_190315.1154.fits	2458558.71818	0.19	11.699	0.403
mml48_190316.1184.fits	2458559.72500	0.68	1.784	0.290
mml48_190317.1150.fits	2458560.70492	0.17	8.322	0.433
mml48_190317.1188.fits	2458560.91069	0.27	26.879	0.267
mml48_190318.1157.fits	2458561.67556	0.65	12.461	0.422
mml48_190318.1190.fits	2458561.88088	0.75	-8.636	0.346
mml48_190319.1150.fits	2458562.65931	0.14	2.734	0.500
mml48_190319.1185.fits	2458562.87245	0.24	22.9002	0.4504
mml48_190320.1168.fits	2458563.72811	0.67	6.241	0.375
mml48_190320.1196.fits	2458563.89865	0.75	-8.893	0.341
mml48_190527.1137.fits	2458631.68671	0.36	37.731	0.398

Table 3: A list of the spectral files used in this project. All spectra were collected at the 1.5m CTIO telescope by Fred Walters. The data is available from Walter's website: `http://www.astro.sunysb.edu/fwalter/`.

2.4.1 Calibration Images

Between 11 and 30 bias images were collected the afternoon before each night of observing. Additionally, dome flat field images were collected most days before sunset in all four filters that were used for observations. After sunset, sky flats were collected, again in all four filters used for observations. As is typical for sky flats, their exposure length varied not only with filter, but also with time, since the sky was gradually darkening as the flats were collected.

Generally, sky flats do a better job of calibrating images than dome flats do [3]. However, dome flats are helpful because they can be collected regardless of cloud cover. Since observations of bright targets can be made through thin cloud cover but flat fields cannot, it is good to have a weather-independent backup calibration image should it be needed.

Night	Flat Fields (Dome)				Flat Fields (Sky)				Science Images				Bias Images
	B	V	R	I	B	V	R	I	B	V	R	I	
1	0	0	0	0	0	0	0	0	0	0	0	0	12
2	11	11	11	11	5	5	4	0	0	0	0	0	23
3	0	0	0	0	6	5	5	5	0	0	151	150	29
4	11	11	11	11	2	0	3	5	66	66	66	65	15
5	11	11	11	11	3	5	3	3	0	0	146	146	26
6	11	11	11	11	5	4	3	4	70	70	70	70	15
7	11	11	11	11	4	4	4	6	0	0	89	88	20
8	11	11	11	11	4	4	4	4	68	67	67	67	15
Total:	66	66	66	66	29	27	26	27	204	203	589	586	155

Table 4: Number of images (flat field, bias, or science) collected in each filter each night. Anywhere there is a 0, there was either no data collected, or the data were discarded.

2.4.2 Science Images

As mention in the Introduction, observing the eclipses of an eclipsing binary in multiple pass bands is essential to making a direct measurement of the stellar properties of a star. In order to satisfy this need, we collected new multi-band photometry of MML 48 at CTIO in March of 2019. We used the .9 meter SMARTS Consortium telescope to make our observations, using the Johnson B and V and Cousins R and I filters. Since the period of MML 48 is close exactly 2 days, each night offered us an opportunity to observe a primary or secondary eclipse. Since the secondary star of MML 48 is so much dimmer than the primary, the secondary eclipses in the B and V bands are extremely faint and well within the error of each measurement, so we decided not to collect any data for the secondary eclipses in these passbands in order to increase the cadence in the R and I bands.

For the primary eclipses, we used B, V, R, and I filters, with exposure times of 40s, 10s, 5s, and 5s respectively. This yielded approximately 250 images per night. Because observations of secondary eclipses did not use two filters, which both had longer exposure times, we collected roughly 300 images on these nights.

3 Data Processing and Analysis

Once the data was collected, we could move onto converting the raw data collected into usable numerical information. In order to carry out the calibration and light curve extractions, I used a program called AstroImageJ. This is a tool created to customize the GUI based ImageJ image processing program for astronomical purposes [5]. Although I used it only to apply calibrations and generate light curves, it has a wide variety of other useful tools for astronomical photometry.

3.1 Calibration of Science Images

Before any data can be extracted from the science images, they all needed to be calibrated in the way described in Section 2.1. This involved applying the bias and flat field images.

Since bias images are not dependant on the filter being used in the telescope, all of these images could be combined together to form one master bias file. This was done by averaging each pixel in each bias image together. An average is ideal for this application because the bias image measures random noise, and we want to subtract a value that best represents that noise, which takes the form of the mean of many different measurements [3]. This master bias file could then be used to calibrate both the flat fields, and the science images directly.

The flat field images required much more care than the bias images. There were two complicating elements: firstly, there are different flats for each filter, and secondly, there were two types of flat to choose from (dome and sky). The multiple-filters aspect arises because there can be dust, debris, and defects in the filter lens itself. Handling this required four different master flats to be generated, one for each filter, as opposed to the one filter-independent master bias.

The choice between the dome and sky flats was more complicated. As described in Table 4, I collected both dome flats and sky flats during my observing run. I elected to use the sky flats for this project by calibrating a small selection of science images in each filter, and determining that the sky flats did a better job of minimizing the amount of deviation in the relative flux of MML 48 when it was not eclipsing. This finding confirmed the conventional choice to use sky flats over dome flats when possible [3].

3.2 Light Curve Extraction

Taking hundreds of calibrated science images does not give us the quantitative measurement of brightness that we need in order to precisely measure the eclipses. In order to draw useful conclusions, we need to convert the images into light curves. A light curve is simply a graph that displays the flux of a star on the y-axis, and the date on the x-axis. If the brightness of a star changes over time, then the light curve will display this.

In order to generate a light curve from all of the images, we need to figure out how bright our target is in each one. The first step in this process is determining out how to measure the brightness of an individual star in an image field. This is accomplished by drawing a circle around the star, and summing the number of counts in each pixel. Then, an annulus is drawn around the target star, as seen in Figure 21. The average number of counts per pixel in this ring is calculated, which gives us a measurement of the ‘brightness’ of the dark night sky. This average can be subtracted from each pixel in the inner circle around our target to remove that background. Doing this for a single star is referred to as *single-aperture photometry*.

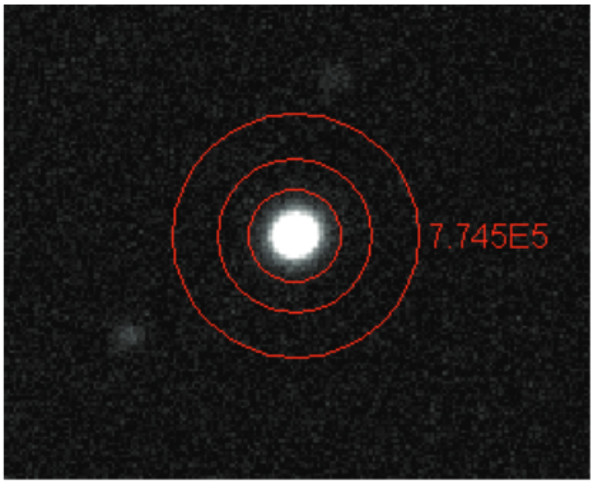

Figure 21: Example of the circle and annulus used to measure a star’s brightness in AstroImageJ from the User Manual [5]. The bright white circle in the center is the target star. The first red circle defines the area in which counts are summed for the target. The area between the second and third circles defines the bounds of the region used to calculate the background counts per pixel. The number in red shows the total number of counts in the target, after the background has been subtracted.

This method suffices when there is no atmospheric variation over time, which is the case for space telescopes like TESS or Hubble. However, variations in airmass, seeing, and cloud cover can change the number of photons that reach the detector between images, which in turn can distort the absolute measure of brightness that we are making by summing the counts. This can be mitigated by instead measuring the relative flux of the target with respect to other nearby stars. This accounts for variance from image to image, as the relationship between the flux of stars will not significantly change because of Earth-based sources of interference. This is called *multi-aperture photometry*, and essentially is comprised of conducting single-aperture photometry on several stars in a field. The relative flux of the target can be calculated using the following equation:

$$\text{Relative Flux} = \frac{\text{Total Target Counts}}{\sum(\text{Total Reference Star Counts})}. \tag{39}$$

By conducting multi-aperture photometry on each science image, one can generate a graph of the relative flux over time: a light curve.

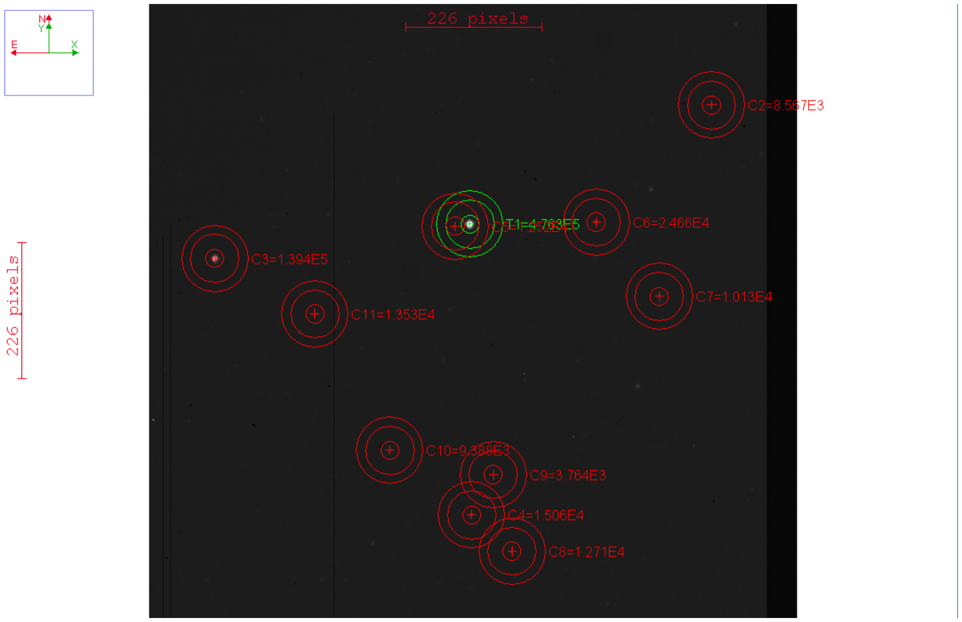

Figure 22: Reference stars considered for use in the multi-aperture photometry of MML 48 (in green), displayed in AstroImageJ. Each star has a circle with a radius of nine, and annulus around that, which were used to determine the relative flux.

3.2.1 Selection of Reference Stars

Finally, I needed to pick which stars in our field to use as references. I selected one primary eclipse and secondary eclipse to use as a representative for the whole dataset, as conducting this analysis on every night's data would have been extremely time consuming and superfluous, as each primary/secondary eclipse was largely the same. I selected the ten brightest stars and generated a table with the corrected number of counts for each reference star, for each science image. The location of the stars used are presented in Figure 22. I then calculated the relative flux of our target with respect to all $(2^{10} - 1)$ possible combinations

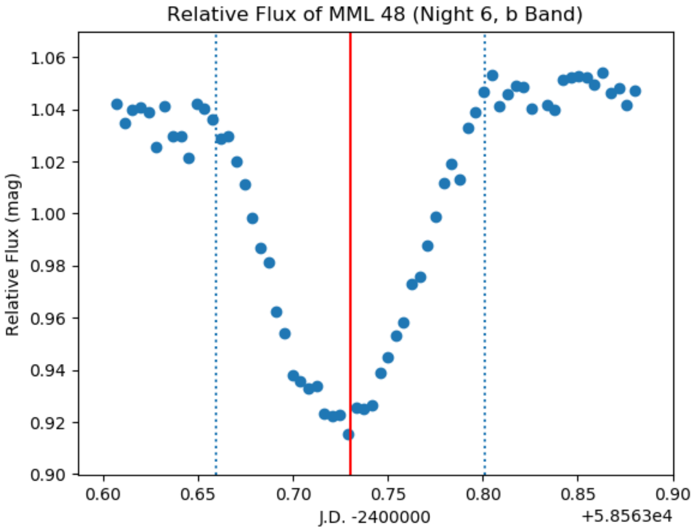

Figure 23: Light curve of MML 48 in the B band from the sixth night of observing. The dashed lines indicate the beginning and end of the eclipse, with the solid red line indicating the peak of the eclipse. The region to the right of the rightmost dashed line is the "plateau region" used in variation calculations. This light curve was produced using the combination of reference stars outlined at the end of Section 0.3.3. The eclipse was recorded to occur at JD - 2400000 = 55987.8836782, with a length of .14166 Julian Days, and all eclipse times were extrapolated from this value.

of reference stars using a python script that iterated over the aforementioned tables. For each night's data, I then selected the data collected after the eclipse ended, and found the standard deviation of that subset, as show in Figure 23.

I compiled all of the standard deviations into one table, and selected the minimum to determine the optimal combination of reference stars for each type of eclipse, on average. The results of this analysis are presented in Figure 24. This figure shows how the deviation changes as different combinations of reference stars are used. While the optimal choice of reference stars varies slightly from filter to filter, it is clear that the choice of all the brightest reference stars (11111) is by no means a bad option, and as far as ease of computation, this choice is ideal. Thus, for all future data analysis, I will use the 5 brightest reference stars.

Note that the analysis presented above only informs the selection of the data analysis parameters: the variations discussed above do not correlate with the errors of the measurements that will be made in the future. They are useful only in determining the optimal choice of reference stars.

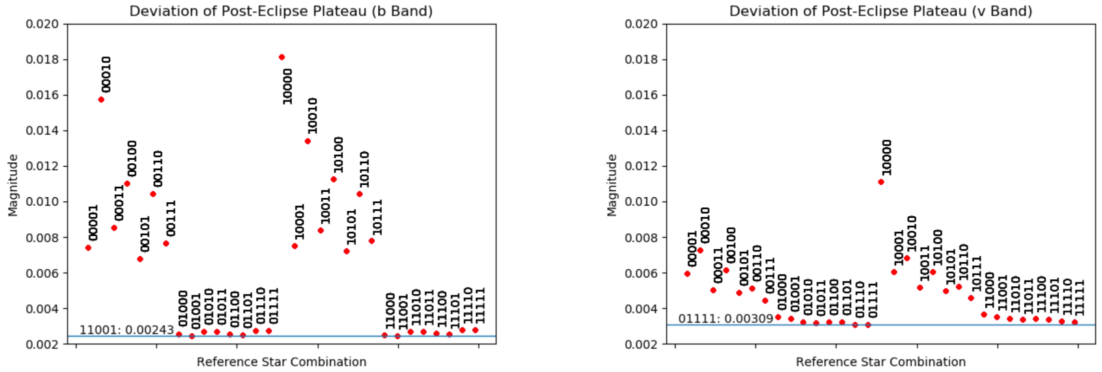

(a) **B** Band

(b) **V** Band

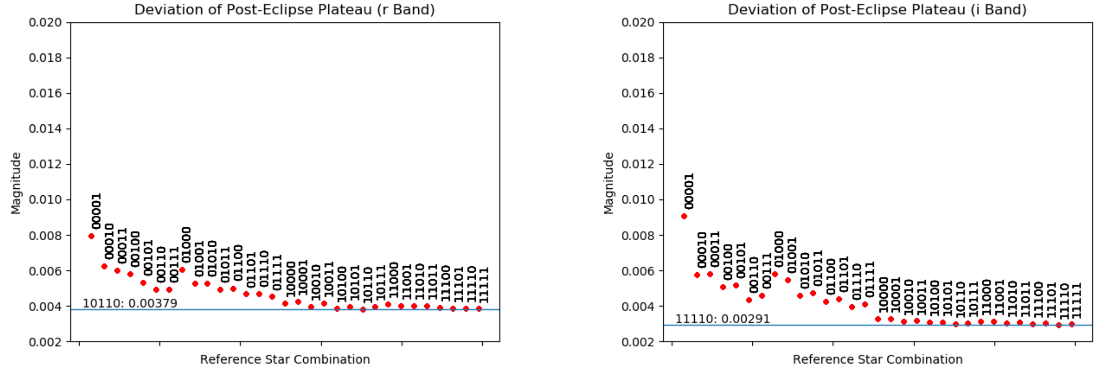

(c) **R** Band

(d) **I** Band

Figure 24: Standard deviation of the plateau region of various combinations of reference stars for a primary eclipse. The text labels indicate which reference stars are being used, where a 1 indicates the reference star is being used, and a 0 indicates that the reference star is being ignored. The horizontal line indicates the minimum deviation for that filter. While 10 stars were initially considered as candidate reference stars, the 5 dimmest rapidly proved to be insignificant, and were discarded, so only 5 reference stars are shown in these plots.

3.2.2 Selection of Aperture and Annulus Radius

Throughout the previous selection of reference stars and choice of flats, a nominal radius of 10 px was used for the generation of relative fluxes. However, this choice was not demonstrably the best radius, so an analysis similar to the one used to determine the ideal set of reference stars was conducted on the radius size. The annulus radius was not varied, since it was entirely determined by the field near MML 48: a small star lies very close by, so the annulus needed to be big enough to avoid that interference.

Filter	Radius (px)					
	7	8	9	10	11	12
B	0.00426	0.00507	0.00433	0.00469	0.00466	0.00511
V	0.00264	0.00330	0.00354	0.00394	0.00465	0.00499
R	0.00475	0.00370	0.00388	0.00425	0.00429	0.00462
I	0.00292	0.00213	0.00188	0.00209	0.00233	0.00245
Mean:	0.00364	0.00355	**0.00341**	0.00374	0.00398	.00429

Table 5: Standard deviation of the relative flux of MML 48 with varying radii. The radius with the lowest mean deviation was with a radius of 9 pixels, so this was the radius used in the multi-aperture photometry. Each standard deviation is a measurement of relative flux, and so has no definite unit. The mean across each filter for each radius is given, with the minimum mean at 9 px shown in bold. This data is presented graphically in Figure 25.

The radius size was determined by calculating the standard deviation in the brightness of MML 48 (while not eclipsing) using various radii choices, using the method outlined in Figure 23. The results of this analysis are presented in Table 5 and Figure 25, which demonstrate that, on average, a radius of 9 px was best. This choice was not cut and dry: the best radius was not the same for each filter, and there was no clear trend describing how the radius impacted the standard deviation for each filter. Although I could have selected a different radius for each filter, that would have introduced a lot of room for error when executing the steps to generate the light curves, so instead I selected the best choice overall.

3.2.3 Selection of Detrending Parameters

After calculating the relative flux of MML 48 for each image, we could move onto the final step in producing our final light curves: detrending. Detrending refers to the process of calculating and removing any trends that an undesired variable might be imposing on a dataset. Typically, the two variables that should be detrended are the airmass and the X/Y position of the target in an image.

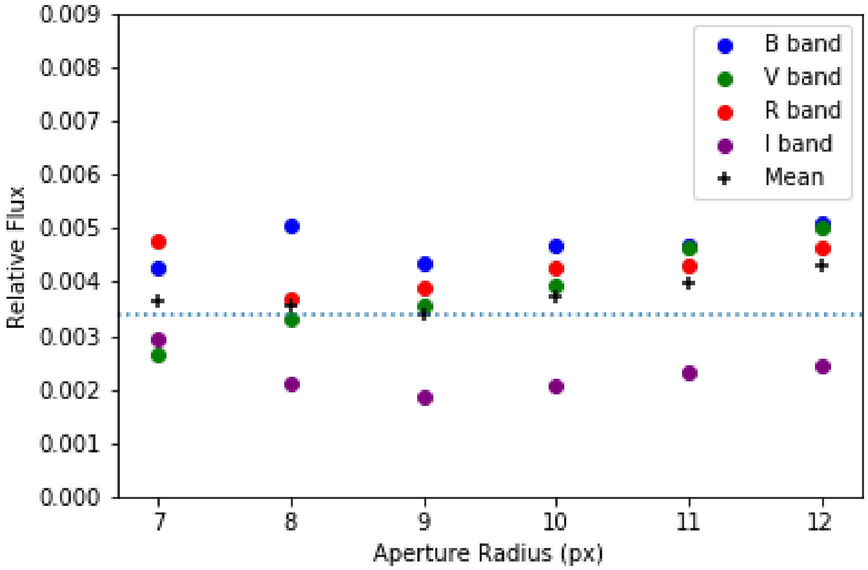

Figure 25: Standard deviation of the relative flux in the out-of-eclipse region with respect to aperture radius. Note that the minimum deviation is not the same for all of the filters: the R and I filters appear to agree on having a minimum around 8-9 px, but the B and V filters do not show a clear minimum.

Airmass is a measurement of the amount of atmosphere between the telescope and outer space. The Earth's atmosphere attenuates and refracts light as it passes through, which needs to be accounted for. The changes in airmass caused by the telescope tracking a target's rise and set can introduce trends into the data that aren't actually created by the target.

The X and Y position of the target in each image matters because, although flat-fielding removes almost all evidence of debris and physical defects on the detector, slight variations can still be present. Ideally the telescope would track the target well enough for the X and Y coordinates to stay the same throughout the night, but in our case, the mount jumped around a fair amount. This also could potentially introduce unwanted trends in the data. Because we know that these artificially introduced trends are present, we can remove them in AstroImageJ. For each night, the light curves were processed with just airmass detrended, both airmass and X/Y detrended, and no detrending. Similar to the choice of radius, the standard deviation of each night's out-of-eclipse region was computed and used as a metric of the usefulness of the detrending. The results of this test are presented in Figure 26. In the end, detrending only airmass resulted in the most cohesive data. This concluded the selection of parameters for the generation of the light curves from the March CTIO observing run.

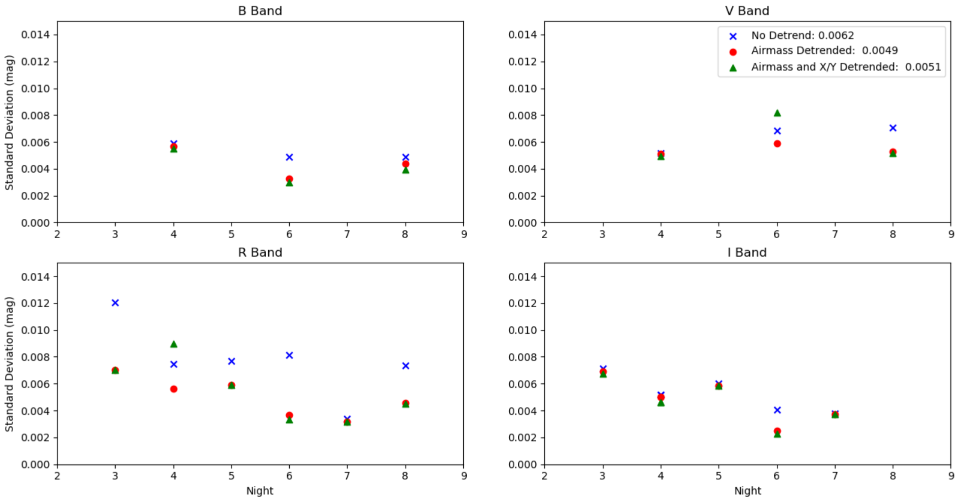

Figure 26: Plot of the standard deviation associated with various detrending options. As seen in all four plots, detrending airmass has an obvious improvement over no detrending. However, the X/Y detrending is less straightforward: while there is a slight improvement for most nights, it actually contributes to the noise on night 6 in the V band and night 4 in the R band. A determination was made that the improvement was so slight on the other nights that X/Y detrending was unnecessary.

3.2.4 Final Light Curves

Using the parameters selected above, the final light curves could be produced. These curves are presented in Figure 27. A truncated table of values for each of the curves is presented in Tables 7 through 10.

3.3 Radial Velocity Curve Extraction

While light curves can provide information about the relative sizes and temperatures of the component stars in an eclipsing binary, spectral data is needed to determine the star's

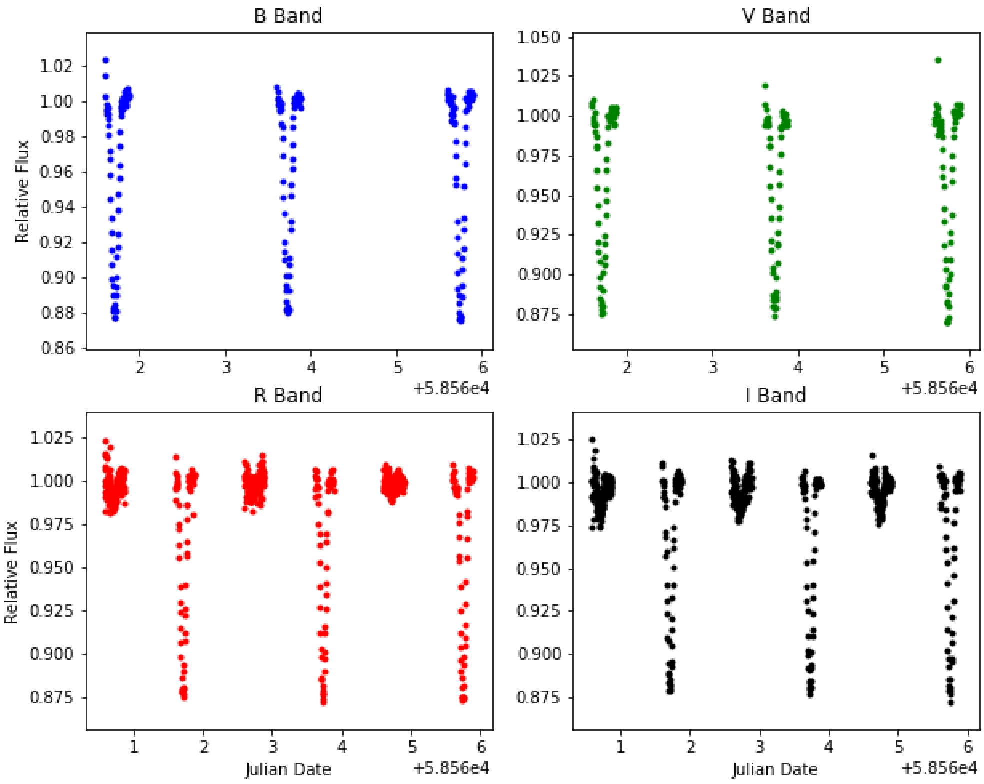

Figure 27: Final light curves from the March 2019 CTIO observing run. There are error bars associated with each data point, but they are obscured by the marker. This data is presented in phase-folded form in Figure 33, along with the model that was eventually generated.

mass ratio, as this data enables one to determine the radial velocities of the components. Radial velocities are extracted by determining the Doppler shift that the stars experience at different phases in their orbits: the stars will become more blue as they approach the observer, and more red as they recede. While in an ideal world we would be able to isolate the spectra of both the primary and secondary star in MML 48, unfortunately it is to dim to be resolved, so we only have one radial velocity curve, from the primary.

The process for determining the Doppler shift requires having a reference star of a similar spectral type that we know the velocity of. While in theory one could determine the velocity of the component stars purely from the location of specific spectra features such as the Hα line, it is much easier to use a known standard star in practice. Each spectra of the target star is overlaid with the matching spectra of the standard, and then the two are *cross-correlated*. In simple terms, this cross-correlation refers to how well the spectra line up. Then, one of the spectra is shifted over by one pixel, and the two are cross-correlated again. This is repeated over a range of pixels, and the 'similarity' of the two spectra are plotted on the y-axis, with the number of pixels offset on the x-axis. At some pixel offset there will be a Gaussian peak where the spectra are most similar, which, by determining the pixel-to-wavelength ratio, gives us a velocity of the target relative to the standard. From there, it is a simple geometric operation of accounting for the Earth's movement (called the *heliocentric correction*) to generate the radial velocities of the target.

3.3.1 Spectral Standards and IRAF

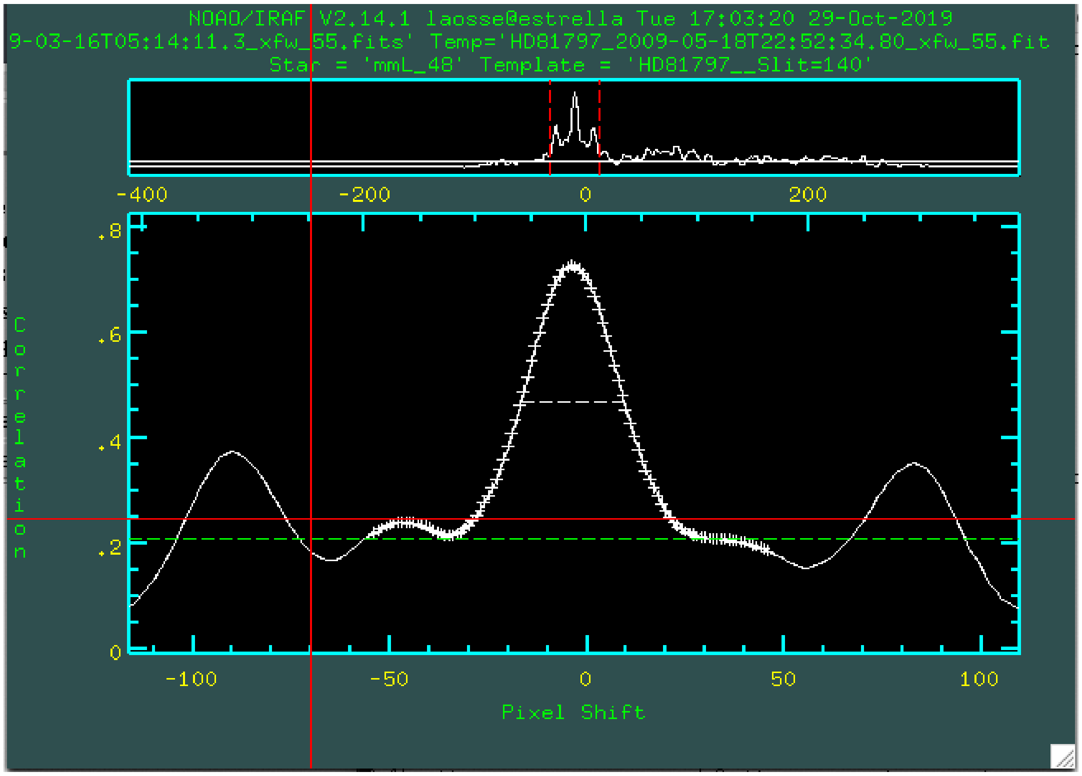

```
          NOAO/IRAF V2.14.1 laosse@estrella Tue 17:03:20 29-Oct-2019
9-03-16T05:14:11.3_xfw_55.fits' Temp='HD81797_2009-05-18T22:52:34.80_xfw_55.fit
                Star = 'mmL_48' Template = 'HD81797__Slit=140'
```

Figure 28: Screenshot of one of the output plots an order being cross-correlated with FXCOR. The large plot in the center shows the rough Gaussian formed by the standard and the target spectra being lined up (solid white line) and the theoretical Gaussian being fit to it (dashed line). Image courtesy of Stefan Laos, Vanderbilt University.

In order to actually compute the radial velocity curves, we needed a suitable spectral standard and a program to compute both the cross-correlation and heliocentric correction. The spectral standard chosen was HD1461: a G-class star (like MML 48) that had been previously analyzed by other members of the research group. The spectra collected in March and the spectral standard were then passed into the IRAF routine FXCOR, which computed a cross-correlation for each order of the echelle spectra. Each order produced a window similar to the one shown in Figure 28, which provided a visual confirmation of what the program was doing. The pixel offset (and by extension the wavelength) is determined from the center of the Gaussian that is fit the cross-correlation, along with an appropriate error measurement. Finally, the Doppler shifting (from the pixel shift) from each order was combined and heliocentrically corrected using a custom IDL script, to get a radial velocity measurement for each spectra. The output of the IDL script can be seen in Figure 29.

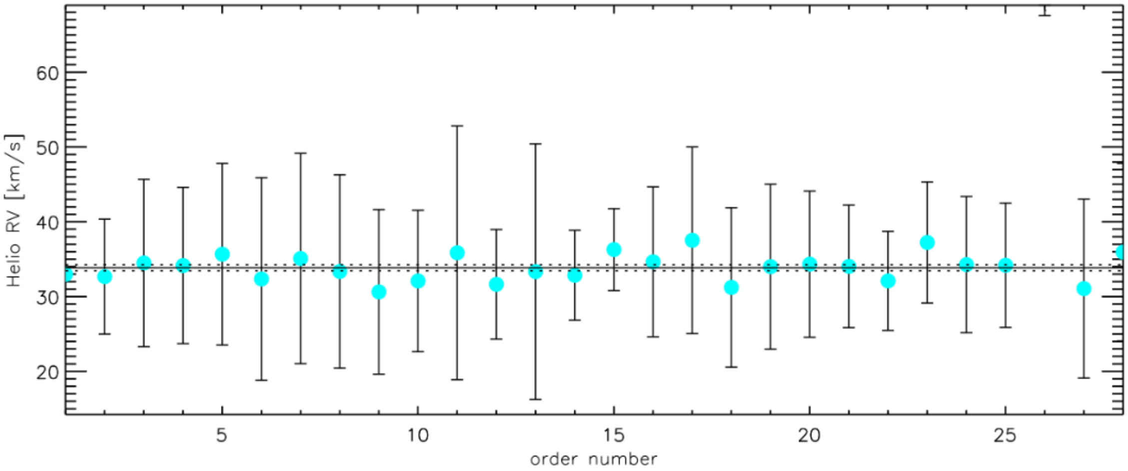

Figure 29: Example output of the IDL script used to combine the radial velocity measurements from various orders into one measurement. The measured radial velocity for each order is shown in blue, and the final mean value and error is shown in the horizontal black lines.

3.3.2 Radial Velocity Curve Generation

With individual radial velocities, it was fairly trivial to generate a radial velocity curve by plotting the radial velocity from each spectra on the y-axis, and the date on the x-axis. The oscillatory nature of the data can better be visualized by phase-folding the data. The radial velocity curves for MML 48 (both raw and phase folded) can be seen in Figure 30.

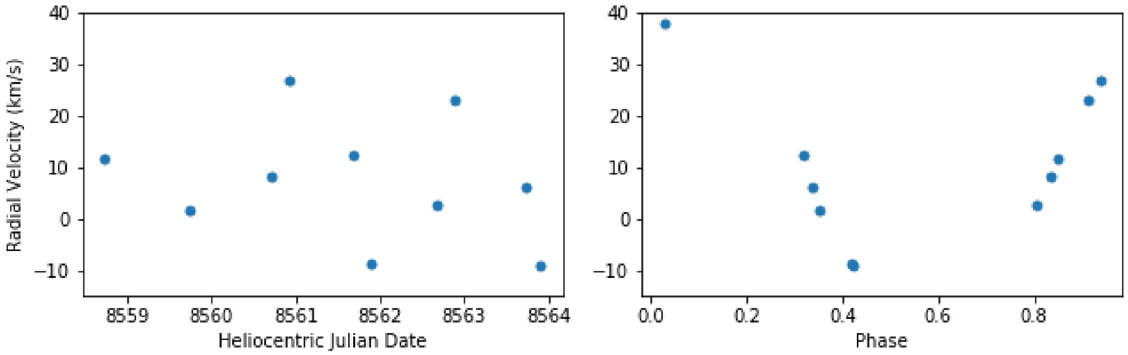

Figure 30: Radial velocities extracted from the 2019 CTIO spectra. The left plot shows the data plotted over date, while the right plot shows the data plotted over phase. In the right plot, the relationship between the radial velocities is much easier to see. Note that the right plot has one point that the left plot does not; one data point was collected several months after the rest, and did not fit on the axes used.

4 Preliminary Modeling

Once I produced the light curves and radial velocity curve, I could move on to making meaningful measurements of the masses and radii of MML 48. As seen in the introduction, the width of the eclipses in combination with the radial velocities of the components can give a precise measurement of the radii of both stars, and of Kepler's laws can be applied to the radial velocities to measure the masses of the component stars. However, this process is not possible for MML 48: as of the writing of this paper, the secondary star's radial velocities have not been resolved, so getting a precise measurement of mass is complicated greatly.

While one could go to the light curves and radial velocities directly to measure the mass and radius, a more rigorous approach is to use a modelling program like PHOEBE 2.1 to generate simulated light curves. By iterating the physical properties of a PHOEBE model until it matches our data, we can converge on a set of values for the mass and radius for each component, with a meaningful assessment of the error associated with those values.

4.1 Integration With Existing Data

The first step in modeling MML 48 was to integrate the data I collected and processed with some of the other data available from prior observations. Namely, existing radial velocities for MML 48 were previously collected by SOAR and FEROS, and can be seen plotted over phase with our SMARTS 1.5m radial velocities in Figure 31. My radial velocity curve appears to agree well with the other data, which indicates that the radial velocity extraction was successful.

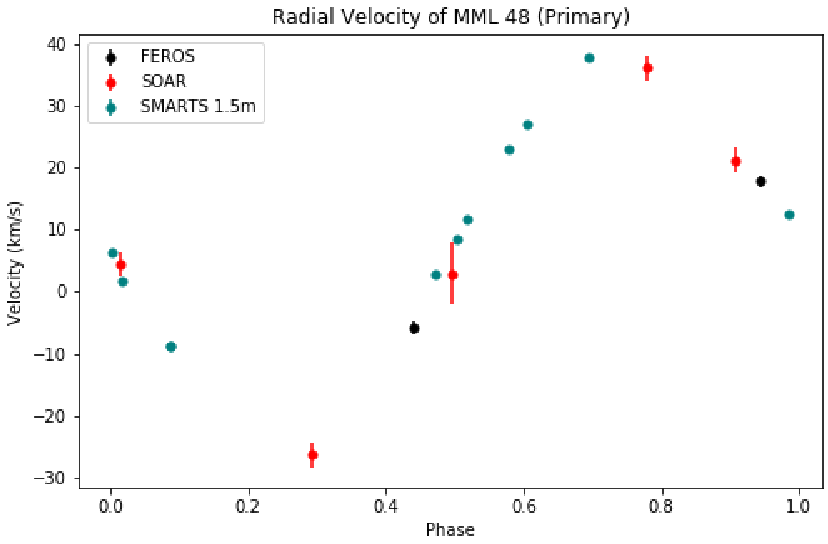

Figure 31: Radial velocities for the primary component of MML 48 plotted over phase. The SMARTS 1.5m was the new data collected at CTIO in March, 2019.

While there are other light curves available (including the ones used to identify MML 48 as an eclipsing system, SuperWASP and ASAS), they were not integrated into this model for a few reasons. First and foremost, the amount of time I had to run my model for was limited, and in the interest of getting results, I used mostly data that I had a hand in processing or collecting. Secondly, the data from SuperWASP and ASAS include the visible range of wavelengths (around the V filter), which I observed myself while at CTIO.

While the redundancy is of course useful for the reduction of error, for my purposes, my own data was sufficiently more resolved as to make these other sources of data not relevant for the scope of this project.

4.2 Spectral Energy Distribution Analysis of MML 48

In addition to the light and radial velocity curves that already existed for MML 48, I had access to Spectral Energy Distribution (SED) analysis for MML 48. An SED analysis is comprised of two parts. First, individual fluxes of a target in different passbands are plotted, as seen in the blue points in Figure 32. Next, a theoretical model for the energy distribution for a star is derived from Stefan-Boltzmann's Law. This model is distorted from an idealized blackbody curve by radiative transfer models to create the bumps that can be seen in Figure 32. This model is then fit to match the photometric data of a the target. The parameters used to generate that fitted model can then be read out and used as a starting point for the overall modeling process.

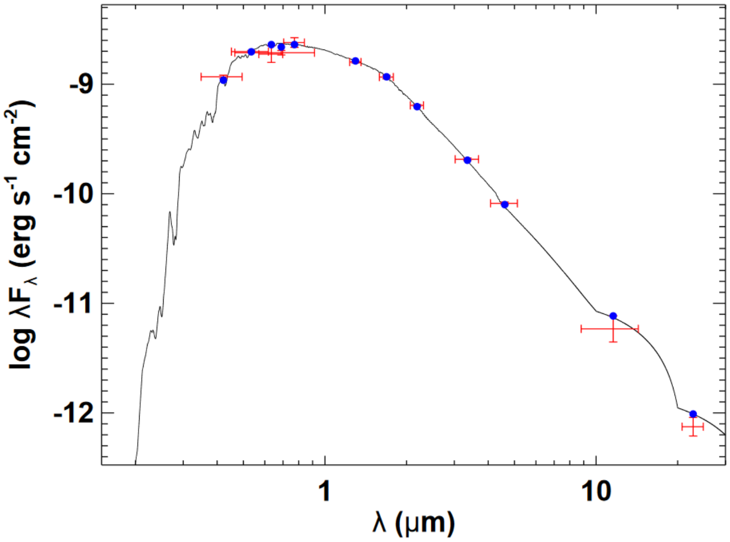

Figure 32: SED analysis of MML 48. The curve is a combination of the emissions from the primary star, which emits light at smaller wavelengths, and the secondary, which emits more in the infrared. The luminosity of the data points is largely dominated by the primary star, but with more infrared measurements, the secondary star's contribution would be more readily observed.

The SED analysis of MML 48 determined the effective temperature of the primary star to be 5500 ± 200 K, which I used as the starting point for my future modeling.

4.3 Generation of Preliminary PHOEBE Model

The first step in the modeling process was to determine what stellar parameters I wanted to measure. In the case of MML 48, I wanted to find the effective temperature of both stars, the inclination of the orbit relative to Earth, the mass ratio, and the radii of both component stars. The primary star's effective temperature already had a good starting point, which simplified the modeling process: I was able to limit how much the model changed this value in order to speed up its run time. While there are many more stellar parameters that PHOEBE can take into account, for the earliest model, these 6 proved to be more than enough work for this project.

Next, we defined the initial values for these parameters, along with all of the other constants that PHOEBE can incorporate, such as the limb darkening function to be used and the surface reflectively of both stars. For the extraneous parameters (the ones not related to the mass, radius, and effective temperature), I used the defaults set by PHOEBE 2. While this does mean that some parameters were optimized for main-sequence stars as opposed to young stars like MML 48, I was informed by the PHOEBE team that these parameters would be sufficient for a preliminary model [Andrej Prša, private communication].

I was able to draw from prior research for the physical parameters. Specifically, an earlier modeling attempt using the SOAR and FEROS radial velocities in addition to the SuperWASP light curves offered a preliminary values for these parameters, which I used as a jumping off point.

With the initial model created from the single-wavelength SuperWASP data and a handful of radial velocity points, I ran a Markov-Chain Monte Carlo (MCMC) sampling to develop a better model that matches the multi-wavelength light curve data and new radial velocities measurements that I obtained in Match 2019. This model consists of a modeled

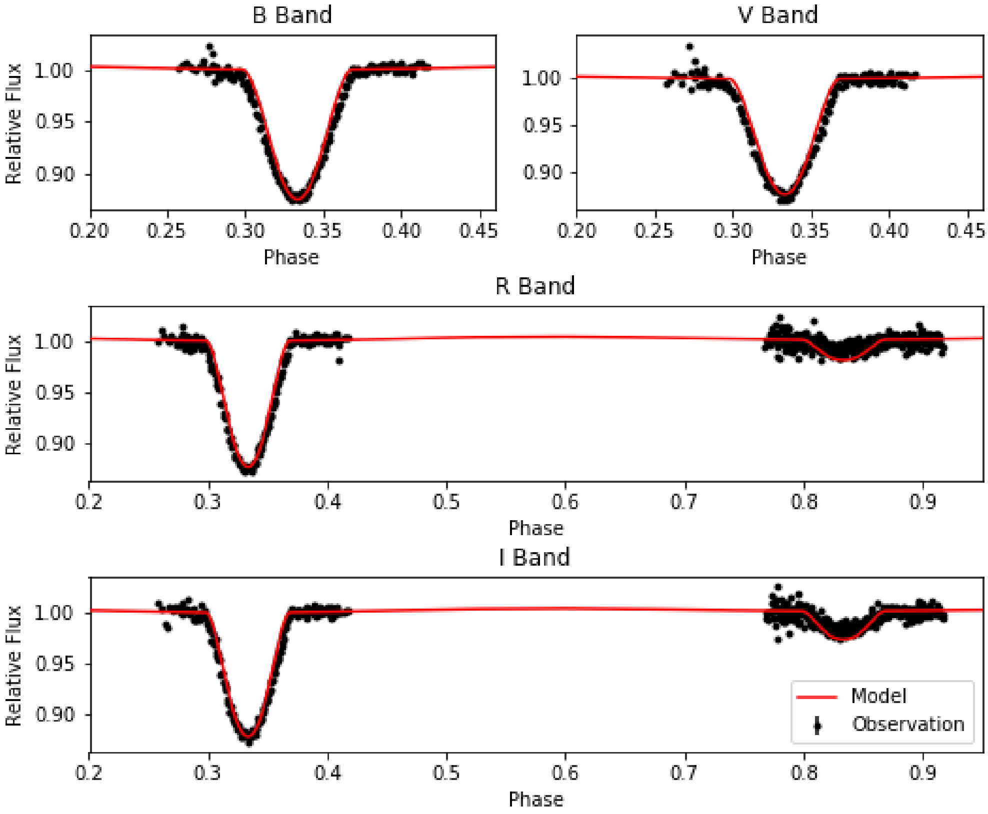

Figure 33: Phase folded modeled light curves for MML 48. The line in red shows the predicted light curve, and the black points show the observed fluxes. In the B and V bands, the secondary eclipse has a very low resolution, and so appears as a triangle instead of a U-shape

radial velocity curve, as well as modeled light curves in all of the filters that I collected data with. These models are presented as the red lines in Figures 34 and 33.

This attempt at optimizing the model largely failed, because an MCMC sampling requires many thousands of steps in order to converge on an optimal solution, and I was only able to run it for 10. This limits the model to serving as a preliminary view of the system, rather than a well-defined set of specific parameters.

While the model shown in Figure 33 might appear to closely match the observed data, careful examination shows that there is a lot of room for improvement: the model's primary eclipses match the data well in all 4 filters, but the secondary eclipses are evidently too deep.

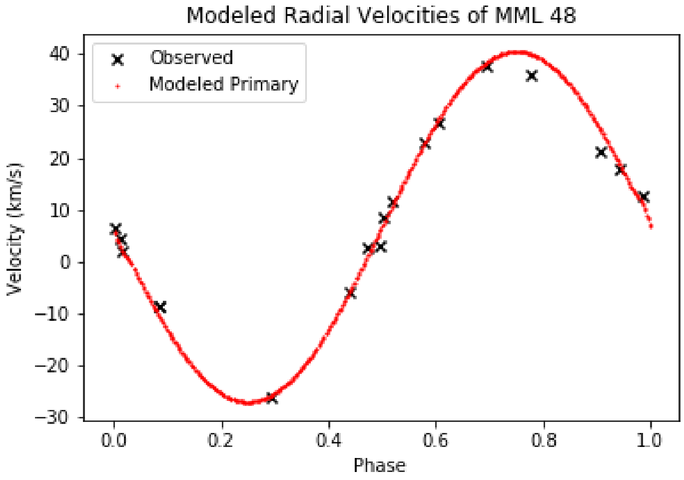

Figure 34: Phase folded modeled radial velocity curves for MML 48.

The secondary eclipses begin at a noticeably higher flux than what the model predicts, which implies that there is some other process happening that the model isn't capturing, such as the imperfections of the initial model carrying through to my final result. Secondly, the depth of the primary eclipses is not quite lined up with the observed data. This implies that either the period or eccentricity from the SuperWASP data was imperfect, which is an important observation. Again, while this might appear to be a sufficiently deviation as to be insignificant, in actuality that small gap represents a fairly large variation in the parameter space explored by the preliminary MCMC optimization. Both of these problems can be solved by allowing the MCMC sampling routine run longer, and allowing the eccentricity and period to be a free parameter in the optimization.

5 Physical Properties for MML 48 From PHOEBE 2.1 Model

The parameters that were used to generate the preliminary PHOEBE 2.1 model used in are presented in Table 6. With a completed model for MML 48, I obtained measurements about the physical properties of the system. Specifically, I derived preliminary measurements for the effective temperatures and radii of both stars, and determine a mass function for the system.

The physical parameters used to generate the PHOEBE 2.1 model are presented in Table 6. There are a few key features to note, mainly the definite measurements of mass present (in spite of the lack of radial velocities for both components), the effective temperatures for the secondary component, the large radii relative to main sequence stars, the inclination being close to $90°$, and the large errors present.

Because the secondary component's radial velocities could not be measured, I cannot give a definitive measurement of the masses for both stars. However, I can compute a mass function for MML 48 with Equation 38 with just the radial velocity of the primary component, the orbital inclination, and the period of the orbit. This mass function serves to constrain the possible combination of masses that are allowed for the system based off of the one radial velocity curve that I do have. Since I have determined values for all of those parameters, the creation of the mass function is a simple exercise in plugging in values and error propagation.

The values used were $2.017 \pm 2 \times 10^{-7}$ days for the period, $31.95 \pm .98\frac{km}{s}$ for the radial velocity, $82.47 \pm .07$ degrees for the inclination, and $6.67 \times 10^{-11}\frac{m^3}{s^2 \cdot kg}$ for Newton's Gravitational Constant. Note that this will return the mass function in terms of kilograms as opposed to solar masses, requiring an extra conversion step. The mass function is then given as

$$\frac{m_2^3}{(m_1 + m_2)^2} = 7.024 \pm .296 \times 10^{-3} M_{\odot}. \tag{40}$$

The masses seen in Table 6 (and the associated mass ratio ≈ 4.3) are just one of the set of masses that are allowed by the mass function for this system. The masses chosen by PHOEBE 2.1 were simply two arbitrary masses close to my starting point that conformed to the mass function given above. Unfortunately, PHOEBE 2.1 uses stellar atmosphere models that are designed for main sequence stars, which means that these masses are quite possibly incorrect, although more data needs to be collected to be sure.

Secondly, the effective temperatures of the stars appear to display some of the limitations of PHOEBE 2.1. The way that PHOEBE computes the flux of a star system in a given set of wavelengths is by using a large lookup table called a *Stellar Atmosphere Model*. These tables provide information about how light from the inside of the star will be impacted by the star's atmosphere and temperature, and are pre-computed by PHOEBE in order to accelerate the run time the model. However, these atmosphere models only exist for certain temperatures. PHOEBE 2.1's default atmosphere model only extends to effective temperatures as low as approximately 3250 K, which is extremely close to the final value that PHOEBE 2.1 computed for MML 48's primary effective temperature. This indicates that, rather than converging on a temperature of 5300 ± 300 K, PHOEBE instead converged on its extreme edge case.

On a supportive note, the mass and radii for the primary component are well within the typical ranges for a pre-main sequence star. The primary has an effective temperature similar to our Sun's (5300k compared to the Sun's 5777K), with a mass close to one $M_{\odot}$. However, the radius is larger than that of the Sun, which implies that MML 48 is still in the contracting phase of stellar birth. This is what one would hope to see with a pre-main sequence star, and does lend credibility to the general correctness of the preliminary model. Additionally, the predicted inclination, $82.47°$, is close to $90°$, as we would expect from a system with deep, well defined eclipses. This also lends credibility to the veracity of the preliminary model.

Finally, since this model was not allowed to run for the extended periods of time needed to effectively utilize an MCMC sampling, the errors associated with each measurement are enormous. These errors can be reduced simply by running the sampling longer.

Parameter	Primary Star	Secondary Star
Period (days)	$2.017 \pm 2\times10^{-7}$	
Orbital inclination (°)	82.47 ± 0.07	
Peak Radial Velocity ($\frac{km}{s}$)	31.95 ± 0.98	
Mass function ($M_\odot$)	$7.024 \pm .296 \times 10^{-3}$	
System Velocity ($\frac{km}{s}$)	6.71 ± 0.07	
Effective Temperature (K)	5300 ± 300	3500 ± 200
Mass ($M_\odot$)	0.93 ± 0.1	0.22 ± 0.05
Radius ($R_\odot$)	1.3 ± 0.1	0.48 ± 0.1

Table 6: Stellar parameters determined by the preliminary PHOEBE model.

6 Conclusions

In spite of these shortcomings, the model does provide some important information. Firstly, it is clear that the model is close to describing MML 48 well, which lends credibility to the earlier modeling and SED analysis. Furthermore, the parameters that PHOEBE 2 generated can be used to get a general idea as to how useful MML 48 will be in training other stellar evolution models in the future.

6.1 MML 48 and the Hayashi Track

As mentioned earlier in this paper, one of the driving reasons to study MML 48 was to add to the short list of fully investigated pre-main sequence eclipsing binaries, in the hopes that the masses and radii measured could be used in future modeling efforts. Because of MML 48's young age, it is particularly useful for empirically testing models on or near the Hayashi Track of stellar development.

As reviewed in Section 1.1, the Hayashi Track is the period of a star's development in which its radius decreases, but its temperature remains mostly constant. Figure 35 shows MML 48's component stars plotted over a series of evolution paths simulated with the Baraffe 2015 stellar evolution model. While of course the Baraffe evolution model is as hobbled as all of the other pre-main sequence stellar evolution models by lack of empirical

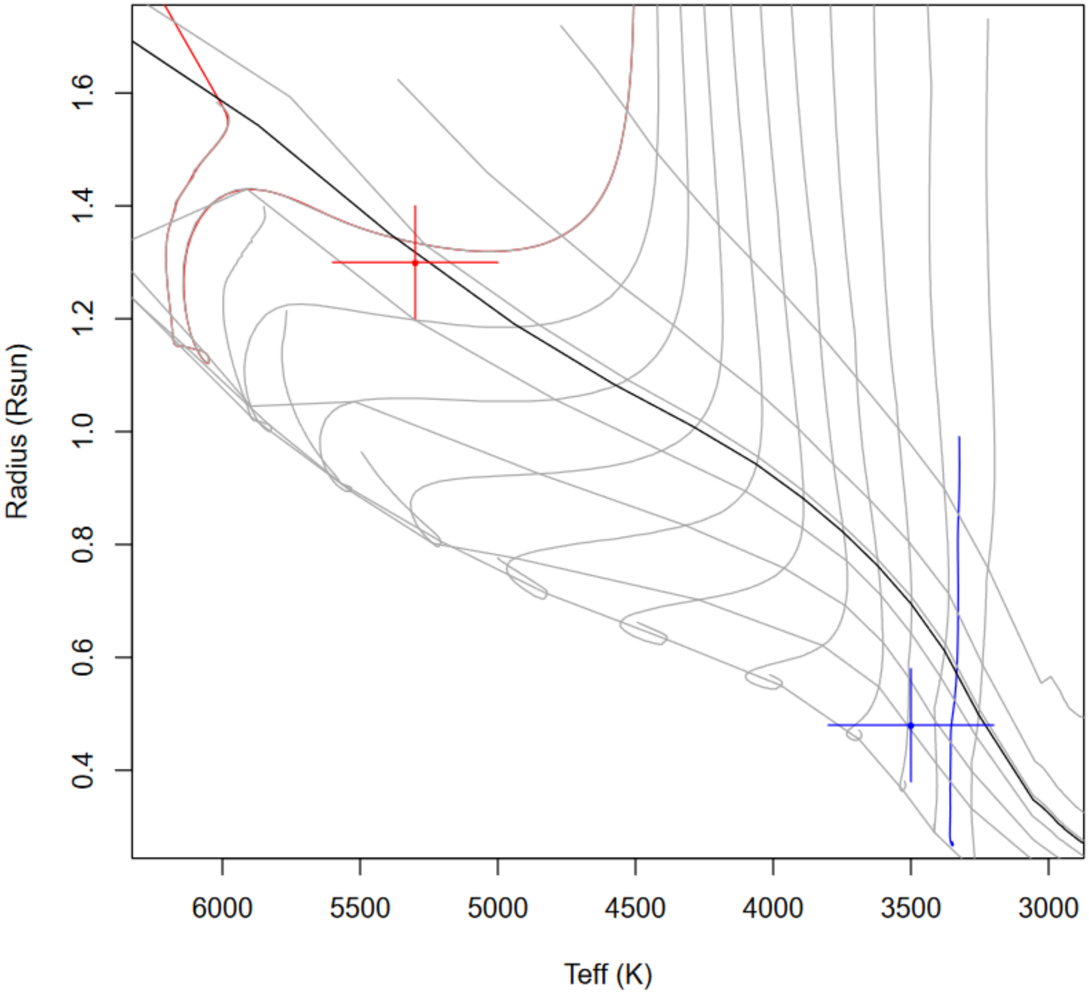

Figure 35: Plot of the primary (red) and secondary (blue) components of MML 48 on an H-R diagram. The grey lines that start vertical are models of how stars approach the main sequence. The vertical section of those lines describes the Hayashi track, where the radius of the star decreases as the temperature remains constant. The diagonal grey lines are isochrones: the age of the star in each model is constant along each line. The line in black shows an isochrone at 16 Myr (the approximate age of MML 48). This H-R diagram uses radius on the y-axis, which is proportional to luminosity, which was used in Figure 1.2.1. The models and isochrones were created using the Baraffe 2015 stellar evolution model.

data, it does give us some rough insight into where MML 48 is in its development.

We can see that, according to this model, the secondary star is still on the Hayashi track, while the primary component has stopped contracting, and is gradually heating up and approaching the main sequence. We can also see that the 16 Myr isochrone (shown in black) lies within the error bars for both the primary and secondary components, which lends some credibility to the model.

6.2 MML 48 and a 16 Million Year Isochrone

In addition to simply contributing to the short list of fully investigated pre-main sequence systems, MML 48 also provides the last piece of data needed to create an *empirical isochrone*. An isochrone is a line that connects different stars with the same age. If the data used to generate that isochrone comes directly from measurements, then that isochrone can be said to be empirically tested, which provides astronomers an invaluable tool in modeling pre-main sequence stellar evolution.

There are two other pre-main sequence eclipsing binaries, named MML 53 and NP PER that are also approximately 15 Myr old, and have masses that are likely significantly different from MML 48's. This means that, in combination with these two other systems, there will be 6 points to define an empirical isochrone at approximately 15 Myr.

6.3 Future Work

The mass function and radii of MML 48 presented in this paper provide only the beginning of the investigation into the properties of MML 48. There are several more avenues of investigation open for MML 48, including the collection of more data, the integration of other existing data into our model, and a more concerted effort towards optimizing the system.

6.3.1 Integration of More Data

A significant area that needs more work is the incorporation of all of the data available to us into our model. There are light curves for MML 48 from a number of other sources in addition to ASAS, SuperWASP, and CTIO. In June of 2018 V and R band light curves were collected at CASLEO in Argentina, and in July 2013 z-band light curves were collected at

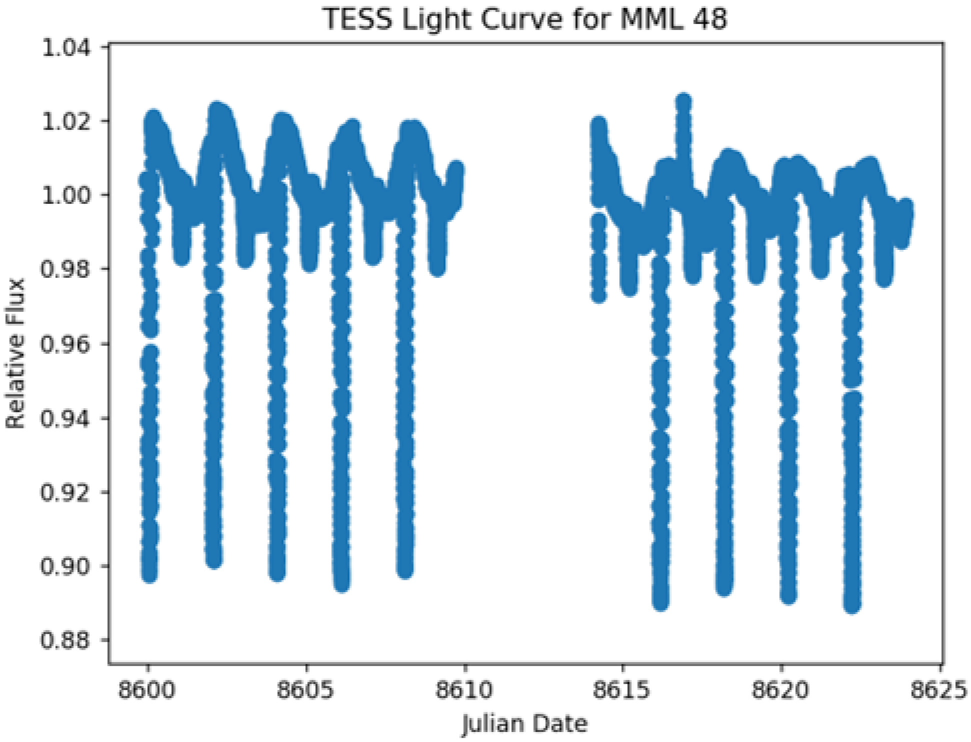

Figure 36: Light curves recorded by the TESS mission. The oscillation in the relative flux between 1.02 and .98 has the characteristics of a star spot, which could potentially be modeled in PHOEBE 2.1. The Julian Date on the X-axis is offset by -2457000 days, as per TESS specifications.

Faulkes Telescope South in Australia. Additionally, more light curves in B, V, R, and I were collected at CTIO in July of 2019, which can be integrated into this model.

Additionally, MML 48 was specified as a target of interest for the Transiting Exoplanet Survey Satellite (TESS), a space telescope that observes the same area in the night sky for two full 13.7 day segments. This data, shown in Figure 36, offers us an extremely good dataset to use for modeling. It also displays some features of MML 48's light curve that were not seen in other data collection runs. For example, there is a large variability in the relative flux of MML 48 unrelated to the eclipses, which was not observed in the ASAS or CTIO photometry.

6.3.2 MCMC Versus Levenberg–Marquardt

A key area to probe further is how the PHOEBE 2.1 model is optimized. Since PHOEBE 2.1 has no native optimization functions, I had to do this step manually. In this project, I used Markov-Chain Monte Carlo optimization, which samples from a probability distribution associated with the model and observed data to eventually converge on a set of parameters for the model that minimizes the difference between the two. I chose this method because it can give me a concrete assessment of the uncertainty of the model, it handles the non-linearity of eclipsing-binary modeling well, and it is a well-accepted method for model optimization in the scientific community.

However, using MCMC methods was not the best approach for this stage of inquiry into MML 48 for a few reasons. Firstly MCMC samplings take a very long time to run when using modeling programs like PHOEBE 2.1. This is because an ideal sampling will create several (ideally hundreds) of models per iteration, and run thousands of iterations to converge on one set of parameters. This requires a large amount of computation time, which turned out to be impractical for this project. Secondly, MCMC samplings are best for finding a set of model parameters when there are few bounds on what the initial parameters should be. Ideally, I would have run several simultaneous MCMC samplings starting from varying places around the parameter space of my model, and wait for them to converge. However, since I already had a good starting place from the prior modeling and SED analysis, I did not make full use of the benefits that MCMC sampling offers. Finally, in order to make meaningful assessments of error from an MCMC sampling, I would have needed to let my optimization run much longer than I had time to allow for.

In retrospect, I should have focused my efforts on using some form of a non-linear least squares fitting approach to model MML 48. Since my initial values for my parameters started close to the final ones, I could have used a more direct minimization approach than MCMC. One good option is using a Levenberg–Marquardt optimization, which uses an iterative non-linear least squares fitting algorithm to converge on a solution. This provides scientifically valid final parameters with meaningful errors, without the need for a full exploration of the parameter space. In the future, I will use such an algorithm to refine my final results.

6.3.3 Future Data

In order to determine the radial velocities needed to determine the exact mass of the component stars in MML 48, a proposal for the collection of infrared spectra of MML 48 was submitted earlier this year. Infrared spectra are particularly desirable because the secondary component of MML 48 is relatively cool, which means that its blackbody curve peaks at a much lower temperature. In the vicinity of 500nm, the secondary star is only 1-2% of the brightness of the primary. However, in infrared the secondary star is approximately 20% of the brightness. This new spectra should allow us to resolve the secondary star's radial velocities, and make a definite measurements of mass.

References

[1] Smarts consortium. URL `http://www.ctio.noao.edu/noao/content/smarts-consortium`.

[2] Jeffrey O. Bennett. *The cosmic perspective*. Pearson Addison-Wesley, San Francisco, CA, 5th ed. edition, 2008. ISBN 978-0-321-50618-4. URL `http://catdir.loc.gov/catdir/toc/ecip0726/2007035821.html`.

[3] D. Scott Birney, Guillermo Gonzalez, and David Oesper. *Observational Astronomy*. Cambridge University Press, 2 edition, 2006. doi: 10.1017/CBO9780511812262.

[4] Bradley W. Carroll and Dale A. Ostlie. *Introduction to Modern Astrophysics*. Pearson, 2006.

[5] Karen A. Collins, John F. Kielkopf, Keivan G. Stassun, and Frederic V. Hessman. ASTROIMAGEJ: IMAGE PROCESSING AND PHOTOMETRIC EXTRACTION FOR ULTRA-PRECISE ASTRONOMICAL LIGHT CURVES. *The Astronomical Journal*, 153(2):77, jan 2017. doi: 10.3847/1538-3881/153/2/77. URL `https://doi.org/10.3847%2F1538-3881%2F153%2F2%2F77`.

[6] R. M. Cutri, M. F. Skrutskie, S. van Dyk, C. A. Beichman, J. M. Carpenter, T. Chester, L. Cambresy, T. Evans, J. Fowler, J. Gizis, E. Howard, J. Huchra, T. Jarrett, E. L. Kopan, J. D. Kirkpatrick, R. M. Light, K. A. Marsh, H. McCallon, S. Schneider, R. Stiening, M. Sykes, M. Weinberg, W. A. Wheaton, S. Wheelock, and N. Zacarias. VizieR Online Data Catalog: 2MASS All-Sky Catalog of Point Sources (Cutri+ 2003). *VizieR Online Data Catalog*, art. II/246, Jun 2003.

[7] F. D'Antona. From protostellar to pre-main-sequence evolution. , 88:574, January 2017.

[8] Trevor J. David, Lynne A. Hillenbrand, Edward Gillen, Ann Marie Cody, Steve B. Howell, Howard T. Isaacson, and John H. Livingston. Age determination in upper scorpius with eclipsing binaries. *The Astrophysical Journal*, 872(2):161, February 2019. doi: 10.3847/1538-4357/aafe09. URL `https://doi.org/10.3847%2F1538-4357%2Faafe09`.

[9] Gaia Collaboration. VizieR Online Data Catalog: Gaia DR2 (Gaia Collaboration, 2018). *VizieR Online Data Catalog*, art. I/345, Apr 2018.

[10] Y. Gómez Maqueo Chew, L. Hebb, H. C. Stempels, A. Paat, K. G. Stassun, F. Faedi, R. A. Street, G. Rohn, C. Hellier, and D. R. Anderson. Fundamental properties of the pre-main sequence eclipsing stars of MML 53 and the mass of the tertiary. , 623:A23, Mar 2019. doi: 10.1051/0004-6361/201833299.

[11] Ejnar Hertzsprung. On the Use of Photographic Effective Wavelengths for the Determination of Color Equivalents. *Publications of the Astrophysical Observatory in Potsdam*, 22:63–63, 1911.

[12] E. Høg, C. Fabricius, V. V. Makarov, S. Urban, T. Corbin, G. Wycoff, U. Bastian, P. Schwekendiek, and A. Wicenec. The Tycho-2 catalogue of the 2.5 million brightest stars. , 355:L27–L30, Mar 2000.

[13] James Hopwood Jeans and George Howard Darwin. I. the stability of a spherical nebula. *Philosophical Transactions of the Royal Society of London. Series A, Containing Papers of a Mathematical or Physical Character*, 199(312-320):1–53, 1902. doi: 10.1098/rsta.1902.0012. URL `https://royalsocietypublishing.org/doi/abs/10.1098/rsta.1902.0012`.

[14] J. Kallrath and E. F. Milone. *Eclipsing Binary Stars: Modeling and Analysis*. IOP Publishing, 2009. doi: 10.1007/978-1-4419-0699-1.

[15] Hannu Karttunen, Pekka Kröger, Heikki Oja, Markku Poutanen, and Karl Johan Donner. *Fundamental Astronomy*. Springer Berlin Heidelberg, 2017. doi: 10.1007/978-3-662-53045-0. URL `https://doi.org/10.1007/978-3-662-53045-0`.

[16] M. Kiraga. ASAS Photometry of ROSAT Sources. I. Periodic Variable Stars Coincident with Bright Sources from the ROSAT All Sky Survey. , 62(1):67–95, Mar 2012.

[17] Eric E. Mamajek, Michael R. Meyer, and James Liebert. Post-T Tauri Stars in the Nearest OB Association. , 124(3):1670–1694, Sep 2002. doi: 10.1086/341952.

[18] Antonia C. Maury and Edward C. Pickering. Spectra of bright stars photographed with the 11-inch Draper Telescope as part of the Henry Draper Memorial. *Annals of Harvard College Observatory*, 28:1–128, Jan 1897.

[19] Semyeong Oh, Adrian M. Price-Whelan, David W. Hogg, Timothy D. Morton, and David N. Spergel. Comoving Stars in Gaia DR1: An Abundance of Very Wide Separation Comoving Pairs. , 153(6):257, Jun 2017. doi: 10.3847/1538-3881/aa6ffd.

[20] Mark J. Pecaut and Eric E. Mamajek. The star formation history and accretion-disc fraction among the K-type members of the Scorpius-Centaurus OB association. , 461 (1):794–815, Sep 2016. doi: 10.1093/mnras/stw1300.

[21] D. L. Pollacco, I. Skillen, A. Collier Cameron, D. J. Christian, C. Hellier, J. Irwin, T. A. Lister, R. A. Street, R. G. West, D. R. Anderson, W. I. Clarkson, H. Deeg, B. Enoch, A. Evans, A. Fitzsimmons, C. A. Haswell, S. Hodgkin, K. Horne, S. R. Kane, F. P. Keenan, P. F. L. Maxted, A. J. Norton, J. Osborne, N. R. Parley, R. S. I. Ryans, B. Smalley, P. J. Wheatley, and D. M. Wilson. The WASP Project and the SuperWASP Cameras. , 118(848):1407–1418, Oct 2006. doi: 10.1086/508556.

[22] Richard Powell. File:hrdiagram.png, May 2011. URL `https://commons.wikimedia.org/w/index.php?curid=1736396`.

[23] A. Prša, K. E. Conroy, M. Horvat, H. Pablo, A. Kochoska, S. Bloemen, J. Giammarco, K. M. Hambleton, and P. Degroote. Physics Of Eclipsing Binaries. II. Toward the Increased Model Fidelity. *The Astrophysical Journal Supplement Series*, 227(2):29, Dec 2016. doi: 10.3847/1538-4365/227/2/29.

[24] Andrej Prša and Tomaz Zwitter. A Computational Guide to Physics of Eclipsing Binaries. Paper I. Demonstrations and Perspectives. *The Astrophysical Journal*, 628, Mar 2005. doi: 10.1086/430591.

[25] Henry Norris Russell. Relations Between the Spectra and Other Characteristics of the Stars. *Popular Astronomy*, 22:275–294, May 1914.

[26] Keivan G. Stassun, Gregory A. Feiden, and Guillermo Torres. Empirical tests of pre-main-sequence stellar evolution models with eclipsing binaries. *New Astronomy Reviews*, 60:1–28, Jun 2014. doi: 10.1016/j.newar.2014.06.001.

[27] J.R. Taylor. *Classical Mechanics*. University Science Books, 2005. ISBN 9781891389221. URL `https://books.google.com/books?id=P1kCtNr-pJsC`.

[28] A. Tokovinin. Chiron overview, Jul 2014. URL `http://www.ctio.noao.edu/noao/content/CHIRON-Overview`.

[29] C. A. O. Torres, G. R. Quast, L. da Silva, R. de La Reza, C. H. F. Melo, and M. Sterzik. Search for associations containing young stars (SACY). I. Sample and searching method. , 460(3):695–708, Dec 2006. doi: 10.1051/0004-6361:20065602.

7 Appendix

7.1 Light Curves (Tables)

JD - 2400000	Relative Flux	Error
58561.59723	1.02286	0.00182
58561.6014	1.01443	0.00181
58561.60556	1.00255	0.00177
58561.60981	0.99399	0.00176
58561.61398	0.99481	0.00175
...	...	...

Table 7: First 5 rows of B band light curves collected at CTIO in March 2019.

JD - 2400000	Relative Flux	Error
58561.59838	1.00812	0.0018
58561.60254	1.00594	0.0018
58561.60671	1.01009	0.0018
58561.61097	0.99962	0.00178
58561.61513	0.99514	0.00177
...	...	...

Table 8: First 5 rows of V band light curves collected at CTIO in March 2019.

JD - 2400000	Relative Flux	Error
58560.58804	1.01539	0.00189
58560.58943	0.99358	0.00185
58560.59127	1.00884	0.00188
58560.59311	0.98215	0.00182
58560.59495	1.02368	0.00191
...	...	...

Table 9: First 5 rows of R band light curves collected at CTIO in March 2019.

JD - 2400000	Relative Flux	Error
58560.59035	1.02507	0.00154
58560.59219	0.9739	0.00148
58560.59403	1.00066	0.00151
58560.59587	0.99133	0.0015
58560.59771	1.0007	0.00151
...	...	...

Table 10: First 5 rows of I band light curves collected at CTIO in March 2019.

7.2 Code

7.2.1 Detrending Comparison

```
from pathlib import Path
import pandas as pd
import numpy as np
import matplotlib.pyplot as plt

JD = 'J.D.-2400000'
path = Path('D:/Astronomy/201903/final_curves/detrends')


files = [
    'n3r.csv',
    'n3i.csv',
    'n4b.csv',
    'n4v.csv',
    'n4r.csv',
    'n4i.csv',
    'n5i.csv',
    'n5r.csv',
    'n6b.csv',
    'n6v.csv',
    'n6r.csv',
    'n6i.csv',
    'n7i.csv',
    'n7r.csv',
    'n8b.csv',
    'n8v.csv',
    'n8r.csv',
    'n4i.csv'
]

def errFind(filepath):
    eclipse_time = 55987.8836782
    eclipse_length = .14166

    # Period of the eclipse divided by two (since we want
       both primary and secondary)
    period = 2.0171078125/2
    df = pd.read_csv(filepath)

    # Determines the time of this eclipse, used to determine
        where the flat sections are
```

```
    while eclipse_time < df[JD][0]:
        eclipse_time = eclipse_time + period
    cutoffup = eclipse_time + (eclipse_length/2)
    cutoffdown = eclipse_time - (eclipse_length/2)
    df = df[(df[JD] > cutoffup) | (df[JD] < cutoffdown) ]
    df = df[df[’rel_flux_T1_n’] > .85]
    df = df[df[’rel_flux_T1_n’] < 1.07]
    print(str(filepath))
    return np.std(df[’rel_flux_T1_n’]), np.std(df[’
       airmass_dn’]), np.std(df[’airmass_xy_dn’])

def getPlotNum(name):
    c = name[2]
    if c == ’b’:
        return 1
    elif c == ’v’:
        return 2
    elif c == ’r’:
        return 3
    else:
        return 4

plt.figure()
nights = [3, 4, 5, 6, 7, 8]
noneTotal = []
airmassTotal = []
xyTotal = []
for filename in files:
    plt.subplot(2, 2, getPlotNum(filename))
    none, airmass, xy = errFind(path / filename)
    noneTotal.append(none)
    airmassTotal.append(airmass)
    xyTotal.append(xy)
    plt.scatter(int(filename[1]), none, color=’blue’, marker
       =’x’)
    plt.scatter(int(filename[1]), airmass, color=’red’,
       marker=’o’)
    plt.scatter(int(filename[1]), xy, color=’green’, marker=
       ’^’)


none =  np.mean(noneTotal)
airmass = np.mean(airmassTotal)
xy = np.mean(xyTotal)
```

```
none = np.round(none, 4)
airmass = np.round(airmass, 4)
xy = np.round(xy, 4)

plt.subplot(2,2,1)
plt.title('B Band')
plt.ylabel('Standard Deviation (mag)')
plt.ylim([0, .015])
plt.xlim([2, 9])

plt.subplot(2,2,2)
plt.legend(['No Detrend: ' + str(none), 'Airmass Detrended:
    ' + str(airmass), 'Airmass and X/Y Detrended:  ' + str(
   xy)])
plt.title('V Band')
plt.ylim([0, .015])
plt.xlim([2, 9])

plt.subplot(2,2,3)
plt.title('R Band')
plt.xlabel('Night')
plt.ylabel('Standard Deviation (mag)')
plt.ylim([0, .015])
plt.xlim([2, 9])

plt.subplot(2,2,4)
plt.title('I Band')
plt.xlabel('Night')
plt.ylim([0, .015])
plt.xlim([2, 9])

plt.show()
```

7.2.2 Reference Table Generation

```
import Normalized_Flux_Generator as nfg
from pathlib import Path
import sys
import os
import pandas as pd
import numpy as np
NIGHTS = [3, 4, 5, 6, 7, 8]

dir = "E:/Astronomy/201903/"

def getStandardDeviationPrimary(nightnum, radius = 10):
    if nightnum % 2 != 0:
        print("Must be an even numbered night.")
        return
    # get the file path to each table
    filedir = dir + "n" + str(nightnum) + "/tables/"
    path = Path(filedir)
    for d in path.iterdir():
        if (str(d).endswith("sky")):
            path = path / "sky"
            break
    print("Generating SDs for b band (night " + str(nightnum
       ) + ")...")
    bdf = pd.DataFrame.from_dict(data=nfg.
       Normalized_Flux_Generator(path/("bband_r" + str(
       radius) + ".csv")).generate(), orient=’index’,
       columns=[’b’])
    print("Generating SDs for v band (night " + str(nightnum
       ) + ")...")
    vdf = pd.DataFrame.from_dict(data=nfg.
       Normalized_Flux_Generator(path/("vband_r" + str(
       radius) + ".csv")).generate(), orient=’index’,
       columns=[’v’])
    print("Generating SDs for r band (night " + str(nightnum
       ) + ")...")
    rdf = pd.DataFrame.from_dict(data=nfg.
       Normalized_Flux_Generator(path/("rband_r" + str(
       radius) + ".csv")).generate(), orient=’index’,
       columns=[’r’])
    print("Generating SDs for i band (night " + str(nightnum
       ) + ")...")
    idf = pd.DataFrame.from_dict(data=nfg.
       Normalized_Flux_Generator(path/("iband_r" + str(
```

```
       radius) + ".csv")).generate(), orient=’index’,
       columns=[’i’])
    bdf[’v’] = vdf[’v’]
    bdf[’r’] = rdf[’r’]
    bdf[’i’] = idf[’i’]
    print("Calculating mean...")
    bdf[’mean’] = bdf.mean(axis=1)
    return bdf

def getStandardDeviationSecondary(nightnum, radius = 10):
    if nightnum % 2 != 1:
        print("Must be an odd numbered night.")
        return
    # get the file path to each table
    filedir = dir + "n" + str(nightnum) + "/tables/"
    path = Path(filedir)
    for d in path.iterdir():
        if (str(d).endswith("sky")):
            path = path / "sky"
            break
    # Combine dicts from each night/filter into one
       dictionary per filter, and find SD of that dict
    print("Generating SDs for r band (night " + str(nightnum
       ) + ")...")
    rdf = pd.DataFrame.from_dict(data=nfg.
       Normalized_Flux_Generator(path/("rband_r" + str(
       radius) + ".csv")).generate(), orient=’index’,
       columns=[’r’])
    print("Generating SDs for i band (night " + str(nightnum
       ) + ")...")
    idf = pd.DataFrame.from_dict(data=nfg.
       Normalized_Flux_Generator(path/("iband_r" + str(
       radius) + ".csv")).generate(), orient=’index’,
       columns=[’i’])
    rdf[’i’] = idf[’i’]
    print("Calculating mean...")
    rdf[’mean’] = rdf.mean(axis=1)
    return rdf


df = pd.DataFrame(columns=[’SDn3’, ’SDn4’, ’SDn5’, ’SDn6’, ’
   SDn7’, ’SDn8’])
for n in NIGHTS:
    if n % 2 == 1:
        tbl = getStandardDeviationSecondary(n)
```

```
        tbl['b'] = np.nan
        tbl['v'] = np.nan
    else:
        tbl = getStandardDeviationPrimary(n)
    df[("SDn" + str(n))] = tbl['mean']
    df[("SDn" + str(n) + 'b')] = tbl['b']
    df[("SDn" + str(n) + 'v')] = tbl['v']
    df[("SDn" + str(n) + 'r')] = tbl['r']
    df[("SDn" + str(n) + 'i')] = tbl['i']
df['mean'] = df.mean(axis=1)
df['mean_b'] = df[['SDn3b', 'SDn4b', 'SDn5b', 'SDn6b', '
   SDn7b', 'SDn8b']].mean(axis=1)
df['mean_v'] = df[['SDn3v', 'SDn4v', 'SDn5v', 'SDn6v', '
   SDn7v', 'SDn8v']].mean(axis=1)
df['mean_r'] = df[['SDn3r', 'SDn4r', 'SDn5r', 'SDn6r', '
   SDn7r', 'SDn8r']].mean(axis=1)
df['mean_i'] = df[['SDn3i', 'SDn4i', 'SDn5i', 'SDn6i', '
   SDn7i', 'SDn8i']].mean(axis=1)
```

7.2.3 Code for Calculation of Normalized Flux from Raw Data Tables

```
import astropy as astro
import numpy as np
import pandas as pd
from pathlib import Path
import sys
import time
import matplotlib.pyplot as plt
JD = 'J.D.-2400000'


class Normalized_Flux_Generator:
    def __init__(self, filename):
        self.filename = filename
        self.results = {}
        self.plateau_cutoff_up = 0
        self.plateau_cutoff_down = 0
        self.use = 'after'

    def normalize_df(self, df, cutup, cutdown, flag):
        before_df = df[df[JD] < cutdown]
        after_df = df[df[JD] < cutup]

        before_df
    def get_combos(self, num_refs):
        combos = []
        for i in np.arange(0, 2**num_refs):
            str = bin(i)[2:]
            while len(str) < num_refs:
                str = "0" + str
            combos.append(str)
        return combos

    def get_normalized_flux(self, df, references):
        i = 2
        temp = pd.DataFrame()
        temp['Source-Sky_T1'] = df['Source-Sky_T1'].copy()
        temp['sum'] = 0
        for t in references:
            if (t == '1'):
                temp['sum'] = temp['sum'] + df['Source-Sky_C
                   ' + str(i)]
            i = i + 1
        rel = (temp['Source-Sky_T1']/temp['sum'])
```

```
        return rel/np.median(rel)

    def convert_combo(self, combo):
        i = 2
        refs = []
        for c in combo:
            if (c == "1"):
                refs.append(’C’ + str(i))
            i = i + 1
        return refs

    def normalized_flux(self, filename, graph = False):

        # Used to estimate how long the task will take to
           run
        TIME_PER_JOB = .01

        # Time of any eclipse, used to calculate the time of
            the given nights eclipse
        eclipse_time = 55987.8836782
        eclipse_length = .14166

        # Period of the eclipse divided by two (since we
           want both primary and secondary)
        period = 2.0171078125/2

        filepath = Path(filename)
        df = pd.read_csv(filepath)

        # Determines how many availible reference stars
           there are
        cols = list(df)
        current_col = cols[16]
        num_refs = 0
        while current_col.startswith("rel_flux_C"):
            num_refs = num_refs + 1
            current_col = cols[16 + num_refs]


        # Determines the time of this eclipse, used to
           determine where the flat sections are
        secondary = False
        while eclipse_time < df[JD][0]:
            eclipse_time = eclipse_time + period
            secondary = not secondary
```

```
self.plateau_cutoff_up = eclipse_time + (
   eclipse_length/2)
self.plateau_cutoff_down = eclipse_time - (
   eclipse_length/2)
df['rel_flux_T1_n'] = self.get_normalized_flux(df, "
   1"*num_refs)
# eliminate outliers
df = df[df['rel_flux_T1_n'] > .85]
df = df[df['rel_flux_T1_n'] < 1.07]


if self.use == 'both':
    ndf = df[(df[JD] > self.plateau_cutoff_up) | (df
       [JD] < self.plateau_cutoff_down)]
elif self.use == 'after':
    ndf = df[(df[JD] > self.plateau_cutoff_up)]
elif self.use == 'before':
    ndf = df[(df[JD] < self.plateau_cutoff_down)]
results = {}
min = 100
for combo in self.get_combos(num_refs):
    if combo != num_refs*"0":
        postdf = ndf[ndf[JD] > self.
           plateau_cutoff_up]
        predf = ndf[ndf[JD] < self.
           plateau_cutoff_down]

        prenormal = self.get_normalized_flux(predf,
           combo)
        postnormal = self.get_normalized_flux(postdf
           , combo)

        prestd = np.std(prenormal)
        poststd = np.std(postnormal)

        if self.use == 'both':
            std = np.average([prestd, poststd],
               weights=[len(prenormal), len(
               postnormal)])
        elif self.use == 'after':
            std = poststd
        else:
            std = prestd

        if std < min:
```

```
                min = std
            results[combo] = std
    print(min)
    return results

def generate(self):
    self.results = self.normalized_flux(self.filename)
    return self.results
```

7.2.4 Observation Plan Generator

```
from astroplan import Observer
import pandas as pd
import numpy as np
import matplotlib.pyplot as plt
import astropy.units as u
from astropy.time import Time
import AltitudePlotter
import os


class Eclisping_Plan_Maker:
    def __init__(self, observatory_name, target_name,
       first_date, utc_offset, num_nights,
       primary_eclipse_time,orbital_period,
       primary_eclipse_time_format = 'jd', template_filename
       ='PLAN_TEMPLATE.tex', output_filename='output.tex'):
        self.observatory_name = observatory_name
        self.target_name = target_name
        self.first_date = Time(first_date)
        self.utc_offset = utc_offset * u.hour
        self.num_nights = num_nights
        self.template_filename = template_filename
        self.output_filename = output_filename
        self.template = open(template_filename, 'r').read()
        self.dir_path = os.path.dirname(os.path.realpath(
           __file__))
        self.orbital_period = orbital_period
        self.primary_eclipse_time = primary_eclipse_time
        self.primary_eclipse_time_format =
           primary_eclipse_time_format

    def _save_altitude_plots(self):
        nights = self.first_date + np.arange(0, self.
           num_nights) * u.day
        names = []
        for night in nights:
          # there was a \ at the end of the next line
            filename = self.dir_path + '/output/figures/' +
               \
                self.target_name.replace(' ', '') + night.
                   value[0:10] + '.jpg'
            print('Generating plot for ' + filename + '...')
            fig = AltitudePlotter.AltitudePlotter(
```

```
           target_name=self.target_name,
           observatory_name=self.observatory_name,
           observing_time=night, utc_offset=self.
           utc_offset, fig=plt.figure())
        fig.set_eclipsing_parameters(Time(self.
           primary_eclipse_time, format=self.
           primary_eclipse_time_format), self.
           orbital_period*u.day)
        plot = fig.plot_altitude()
        plot.savefig(filename)
        plt.close(plot)
        names.append('figures/' + self.target_name.
           replace(' ', '') + night.value[0:10] + '.jpg'
           )
    return names

def _get_figure_laTex(self, names):
    result = ''
    for name in names:
        print('Generating TeX for ' + name + '...')
        result = result + self._get_include_graphics(
           name)
    return result

def _get_include_graphics(self, filename, caption='
   Caption Here'):
    return '\\begin{center}\n\t\\begin{figure}[h]\n\t\t
       \\centering\n\t\t\\includegraphics[width=4in]{' +
        filename + '}\n\t\t\\caption{' + caption + '}\n\
       t\t\\label{' + filename + '}\n\t\\end{figure}\n\\
       end{center}\n'

def _get_times_table(self, observatory_name, first_date,
    utc_offset, num_nights):

    obs = Observer.at_site(observatory_name)
    nights = first_date + np.arange(0, num_nights) * u.
       day

    df = pd.DataFrame(columns=['Date', 'Sunset',
                               'N. Twilight (Evening)',
                                  'N. Twilight (Morning)
                                  '])

    # Add target rise/target set
```

```
        # Add eclipse entry/exit
        night_names = list(map(lambda x: x.value[0:10],
           nights))
        df.Date = night_names


        sunset = obs.sun_set_time(nights)
        sunset.format = 'iso'
        df['Sunset'] = list(map(lambda time: time.value
           [11:19], sunset))

        evening_twilight_dates = obs.
           twilight_evening_nautical(
            nights)
        evening_twilight_dates.format = 'iso'
        df['N. Twilight (Evening)'] = list(
            map(lambda date: date.value[11:19],
               evening_twilight_dates))

        morning_twilight_dates = obs.
           twilight_morning_nautical(
            nights)
        morning_twilight_dates.format = 'iso'
        df['N. Twilight (Morning)'] = list(
            map(lambda date: date.value[11:19],
               morning_twilight_dates))
        return df.to_latex(index=False)

    def generate_latex(self):
        timetable = self._get_times_table(observatory_name=
           self.observatory_name,
                                          first_date=self.
                                             first_date,
                                             utc_offset=self
                                             .utc_offset,
                                             num_nights=self
                                             .num_nights)
        altplots = self._get_figure_laTex(self.
           _save_altitude_plots())

        print('Generating LaTeX File...')
        output = self.template.replace('!TIMETABLE!',
           timetable)
        output = output.replace('!ALTPLOTS!', altplots)
        output = output.replace('!STARTDATE!', self.
```

```
            first_date.value[0:10])
        output = output.replace(
            '!ENDDATE!', (self.first_date + self.num_nights*
                u.day).value[0:10])
        output = output.replace('!OBJECT!', self.target_name
            )

        print('Writing to ' + self.output_filename + '...')
        open(self.dir_path + '/output/' +
             self.output_filename, 'w').write(output)


Eclisping_Plan_Maker(observatory_name='Cerro Tololo',
    target_name='MML 48',
            first_date='2019-07-03 00:00', utc_offset=0,
                num_nights=5, primary_eclipse_time
                =2454945.0393516, orbital_period =
                2.0171078125).generate_latex()
```

7.2.5 Time Table Generator

```
from astroplan import Observer
import pandas as pd
import numpy as np
import astropy.units as u
from astropy.time import Time
from astroplan import FixedTarget

observatory_name = ’Cerro Tololo’
num_nights = 5
first_date = ’2019-07-03 00:00’

obs = Observer.at_site(observatory_name)
nights = first_date + np.arange(0, num_nights) * u.day
target = FixedTarget.from_name(’MML 48’)

df = pd.DataFrame(columns=[’Date’, ’Sunset’,
    ’N. Twilight (Evening)’, ’N. Twilight (Morning)’, ’
       Ingress’, ’Egress’])

# Add target rise/target set
# Add eclipse entry/exit
night_names = list(map(lambda x: x.value[0:10], nights))
df.Date = night_names


sunset = obs.sun_set_time(nights)
sunset.format = ’iso’
df[’Sunset’] = list(map(lambda time: time.value[11:19],
   sunset))

evening_twilight_dates = obs.twilight_evening_nautical(
    nights)
evening_twilight_dates.format = ’iso’
df[’N. Twilight (Evening)’] = list(
    map(lambda date: date.value[11:19],
       evening_twilight_dates))

morning_twilight_dates = obs.twilight_morning_nautical(
    nights)
morning_twilight_dates.format = ’iso’
df[’N. Twilight (Morning)’] = list(
    map(lambda date: date.value[11:19],
       morning_twilight_dates))
```

```
print(obs.target_rise_time(nights, target, which='next'))
# print(df.to_latex(index=False))
# return df.to_latex(index=False)
```